NAVAL POSTGRADUATE SCHOOL
Monterey, California

THESIS

ON THE CALCULATION OF PARTICLE TRAJECTORIES FROM SEA SURFACE CURRENT MEASUREMENTS AND THEIR USE IN SATELLITE SEA SURFACE PRODUCTS OFF THE CENTRAL CALIFORNIA COAST

by

Luke J. Spence

December 2007

Thesis Advisor:	Francis X. Giraldo
Co-Advisor:	Jeffrey Paduan

THIS PAGE INTENTIONALLY LEFT BLANK

REPORT DOCUMENTATION PAGE

Form Approved OMB No. 0704-0188

1. AGENCY USE ONLY (*Leave blank*)	2. REPORT DATE	3. REPORT TYPE AND DATES COVERED
	December 2007	Master's Thesis

4. TITLE AND SUBTITLE On the Calculation of Particle Trajectories from Sea Surface Current Measurements and their Use in Satellite Sea Surface Products off the Central California Coast

5. FUNDING NUMBERS

6. AUTHORS Spence, Luke J.

7. PERFORMING ORGANIZATION NAME(S) AND ADDRESS(ES)
Naval Postgraduate School
Monterey CA 93943-5000

8. PERFORMING ORGANIZATION REPORT NUMBER

9. SPONSORING/MONITORING AGENCY NAME(S) AND ADDRESS(ES)

10. SPONSORING/MONITORING AGENCY REPORT NUMBER

11. SUPPLEMENTARY NOTES The views expressed in this thesis are those of the author and do not reflect the official policy or position of the Department of Defense or the U.S. Government.

12a. DISTRIBUTION/AVAILABILITY STATEMENT
Approved for public release; distribution is unlimited.

12b. DISTRIBUTION CODE

13. ABSTRACT(*maximum 200 words*)

This thesis explores the possibility and feasibility of improving existing satellite measurements of sea surface temperature (SST) by the incorporation of high-frequency (HF) radar-derived surface current data. Water parcels tagged with SST are advected using particle trajectories calculated by integrating surface current velocity data. The SST of these advected water parcels are compared to SST measurements at the final times and locations of the advected water parcels. Different methods of generating surface currents from HF radar measurements are also examined. The Totals current method is a local fitting method which generates surface current measurements by solving a least-squares equation fitting multiple measurements from different radar sites. The Open-boundary Modal Analysis (OMA) method is a global method which fits a series of eigenfunction modes to available radial measurements. These modes are generated by solving two Laplacian eigenvalue problems on the domain with Dirichlet and Neumann boundary conditions, and adding a set of boundary modes to account for flow across open boundaries. Any current field in the domain can be described using a combination of these modes. The two methods are compared for accuracy against an analytic solution to the linear Stommel problem.

14. SUBJECT TERMS	15. NUMBER OF PAGES
Sea Surface Temperature, CODAR HF Radar, Open-Boundary Modal Analysis, Vector Field Decomposition, Eigenfunction Expansion	88
	16. PRICE CODE

17. SECURITY CLASSIFICATION OF REPORT	18. SECURITY CLASSIFICATION OF THIS PAGE	19. SECURITY CLASSIFICATION OF ABSTRACT	20. LIMITATION OF ABSTRACT
Unclassified	Unclassified	Unclassified	UU

NSN 7540-01-280-5500

Standard Form 298 (Rev. 2-89)
Prescribed by ANSI Std. 239-18 298-102

THIS PAGE INTENTIONALLY LEFT BLANK

Approved for public release; distribution is unlimited

ON THE CALCULATION OF PARTICLE TRAJECTORIES FROM SEA SURFACE CURRENT MEASUREMENTS AND THEIR USE IN SATELLITE SEA SURFACE PRODUCTS OFF THE CENTRAL CALIFORNIA COAST

Luke J. Spence
Lieutenant, National Oceanic and Atmospheric Administration
B.S., Colorado School of Mines, 2002

Submitted in partial fulfillment of the
requirements for the degree of

MASTER OF SCIENCE IN APPLIED MATHEMATICS

from the

NAVAL POSTGRADUATE SCHOOL
December 2007

Author: Luke J. Spence

Approved by: Francis Giraldo, Advisor

Jeffrey Paduan, Co-Advisor

Clyde Scandrett, Chairman
Department of Applied Mathematics

THIS PAGE INTENTIONALLY LEFT BLANK

ABSTRACT

This thesis explores the possibility and feasibility of improving existing satellite measurements of sea surface temperature (SST) by the incorporation of high-frequency (HF) radar-derived surface current data. Water parcels tagged with SST are advected using particle trajectories calculated by integrating surface current velocity data. The SST of these advected water parcels are compared to SST measurements at the final times and locations of the advected water parcels. Different methods of generating surface currents from HF radar measurements are also examined. The Totals current method is a local fitting method which generates surface current measurements by solving a least-squares equation fitting multiple measurements from different radar sites. The Open-boundary Modal Analysis (OMA) method is a global method which fits a series of eigenfunction modes to available radial measurements. These modes are generated by solving two Laplacian eigenvalue problems on the domain with Dirichlet and Neumann boundary conditions, and adding a set of boundary modes to account for flow across open boundaries. Any current field in the domain can be described using a combination of these modes. The two methods are compared for accuracy against an analytic solution to the linear Stommel problem.

THIS PAGE INTENTIONALLY LEFT BLANK

TABLE OF CONTENTS

I. BACKGROUND 1

A. REMOTE SENSING 1

B. CLOUDINESS ON THE CENTRAL CALIFORNIA COAST . . 2

C. INCLUSION OF CURRENT DATA IN SST MODEL 3

D. THESIS OBJECTIVES 4

II. THEORY 7

A. SST MODEL 7

B. DESCRIPTION OF HF RADAR 8

C. TOTALS SURFACE CURRENT METHOD 10

D. OPEN MODAL ANALYSIS METHOD 15

1. Calculation of Modes 16

2. Unstructered Grid 21

3. Fitting Current Data to OMA Modes 21

E. PARTICLE TRAJECTORIES 24

III. METHODS 27

A. MODEL VALIDATION AND SST COMPARISONS 27

B. DATA USED 30

1. SST Data 30

2. HF Radar Data 31

C. CASE STUDIES 31

1. CENC Domain 31

2. Dates of Study 31

3. Stommel Ocean Model 32

D. MATLAB PROCESSING 36

1. Processing of Radial Data 37

2. Processing to Totals Currents 37

3. OMA Modes Processing 38
4. Fitting Radial Data to OMA Modes 41
5. Particle Trajectories 41
IV. RESULTS 45
A. STOMMEL MODEL CURRENTS 45
1. Current Statistics 45
2. Totals Currents Reconstruction 46
3. OMA Currents Reconstruction 47
4. Mode Coefficient Penalty 49
B. SST COMPARISONS AND MODEL TESTING 51
1. Comparison of OMA and Totals Advected Methods . . . 57
2. Calculations on the Distance of Advected Particles 60
C. RECONSTRUCTION OF SST FIELD 60
D. RECOMMENDATIONS FOR FURTHER STUDY 63
1. Refinement of Advection Model 63
2. Frontal Advection 63
3. Lagrangian Coherent Structures 63
4. Adaptive Interpolation Functions for Scattered Data Interpolation 64
5. Improvements to Current Fits from OMA Method 66
APPENDIX. 67
LIST OF REFERENCES 69
INITIAL DISTRIBUTION LIST 71

LIST OF FIGURES

1. Cloudiness on the central California coast. 2
2. SST and current field in Monterey Bay on 19:10 GMT, January 9, 2007. 4
3. Illustration of Totals method 9
4. GDOP error illustration 11
5. Current field for CENC region on 06:00 GMT, 19 October, 2006. 13
6. GDOP error as a function of angle separation 15
7. Rectangular and Triangular Grids 22
8. Flow chart of SST comparison procedure. 28
9. Advected SST comparison 29
10. Static SST comparison 29
11. Random SST comparison 30
12. Radar coverage for the CENC region 33
13. Stommel Ocean model and sample HF Radar domain 35
14. Triangular Mesh for CENC region. 39
15. Close-up of Triangular Mesh for the Monterey Bay. 40
16. Dirichlet modes for CENC domain 42
17. Neumann modes for CENC domain 43
18. Boundary modes for CENC domain 44
19. Reconstruction of Stommel current field using Totals method 47
20. Reconstruction of Stommel current field using OMA method 48
21. Stommel currents reconstructed from different OMA modes 50
22. κ study for Stommel domain 51
23. SST comparison for Totals currents for January, 2007 52
24. SST comparison for OMA currents for January, 2007 52
25. SST comparison for Totals currents for October, 2006 53
26. SST comparison for OMA currents for October, 2006 53

27. SST anomaly comparison for Totals currents for January, 2007 54
28. SST anomaly comparison for OMA currents for January, 2007 54
29. SST anomaly comparison for Totals currents for October, 2006 55
30. SST anomaly comparison for OMA currents for October, 2006 55
31. SST comparison for OMA and Totals currents for January, 2007 58
32. SST anomaly comparison for OMA and Totals currents for January, 2007 58
33. SST comparison for OMA and Totals currents for October, 2006 59
34. SST anomaly comparison for OMA and Totals currents for October, 2006 59
35. Displacement of advected particles 61
36. Recontructed SST field 62
37. Lagrangian Coherent Structure 64
38. Gaussian weighting function. 65
39. Gaussian weighting function, slimmed in the x direction. 66

LIST OF TABLES

I. Statistics for Totals Currents calculated on Stommel domain. 45
II. Statistics for OMA Currents calculated on Stommel domain. 46
III. Satellite Images used in the January, 2007 Case Study 67
IV. Satellite Images used in the October, 2006 Case Study 68

THIS PAGE INTENTIONALLY LEFT BLANK

ACKNOWLEDGMENTS

Thanks to my advisors, Frank Giraldo and Jeff Paduan for their invaluable guidance. Thanks to the leadership at the NOAA, Southwest Fisheries Science Center, Environmental Research Division, for making my studies at NPS possible. A special thanks also to Dr. David Kaplan for his assistance with the current and trajectory processing. Without David's MATLAB toolboxes and help, the processing in this thesis would not be possible. Most of all, thanks to my incredible wife Lisa, who supported me during the long nights writing this thesis by feeding me, walking the dog, and reminding me how to take a derivative. Psalm 115:1.

THIS PAGE INTENTIONALLY LEFT BLANK

I. BACKGROUND

A. REMOTE SENSING

Remote sensing is the measurement of a property of an object by a sensor not in direct contact with the object being measured. Remote sensing techniques extend important tools for scientists measuring the Earth's environment. Many established measurement techniques have been adapted to fit on remote sensing platforms, including satellites, fixed land-based platforms, Unmanned Aerial Vehicles (UAVs), Autonomous Underwater Vehicles (AUVs), or the underside of manned aircraft. These remote sensing techniques offer vast improvements over traditional measurement and sampling techniques in the possible spatial domain of measurement and cost effectiveness of measurement. The National Oceanic and Atmospheric Administration (NOAA) has launched numerous environmental satellites with the goal of providing remote sensing of the Earth and its atmosphere.

These satellites hold multiple sensors onboard, each designed to measure different environmental parameters. Many of the sensors designed to take a measurement of the earth's surface cannot do so when clouds block the sensor's view of the earth's surface. Passive radiative sensors, such as the Advanced Very High Resolution Radiometer (AVHRR), are particularly prone to this problem. The AVHRR sensor provides a measurement of sea surface temperature (SST) from onboard NOAA's Polar Operational Environmental Satellites (POES). Cloudiness presents significant problems in geographical areas with persisting cloud cover or fog banks, such as California's central and northern coasts. The measurement ability of satellites in the presence of clouds might be improved by the additional information provided by measurements that are not affected by cloud presence.

B. CLOUDINESS ON THE CENTRAL CALIFORNIA COAST

To illustrate just how bad the cloud problem can be in the central and northern California coast, statistics were calculated on the region covered by the California Ocean Currents Monitoring Program (COCMP) High Frequency Radars (hereafter called the CENC region). Individual satellite pass data from the NOAA POES AVHRR sensor were downloaded (courtesy of the NOAA CoastWatch, West Coast Regional Node) and masked to exclude any SST pixels not within the CENC region. The percentage of cloudy pixels within the region was calculated for each satellite pass.

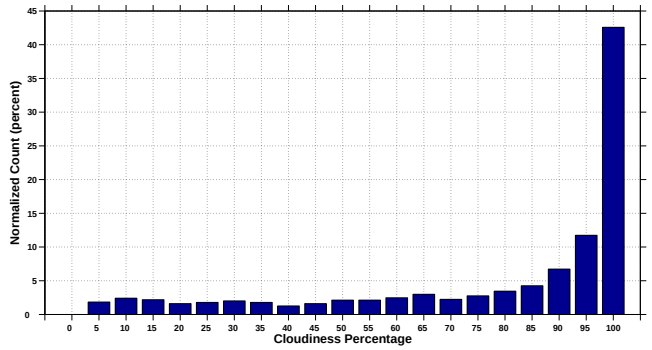

(*a*)

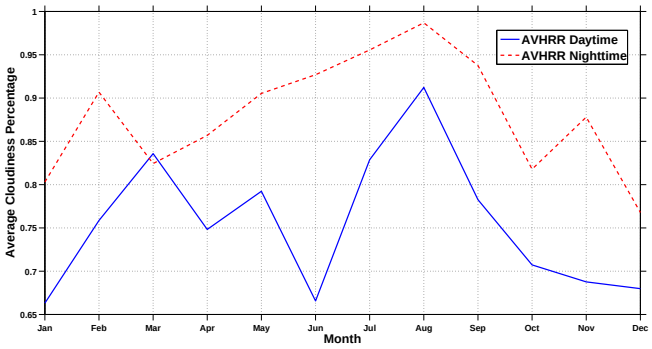

(*b*)

Figure 1. Cloudiness on the central California coast (CENC region). ***a.*** Normalized histogram of cloudiness percentage for individual satellite passes. ***b.*** Average cloudiness of individual satellite passes as a function of month.

A total of 1,966 satellite images were analyzed from Jan 1, 2006 to August 10, 2007. Figure 1a shows a histogram (normalized by the total number of satellite images) of the cloudiness percentage for all the satellite images as well as average cloudiness as a function of month. The histogram is skewed to the far right, indicating that the majority of SST images within the CENC domain have vast amounts of their data destroyed by clouds. Day and night satellite images were separated in Figure 1b due to the different cloudmasking used in the SST processing. The nighttime cloudmasking algorithm only uses infrared bands, while the daytime cloudmasking algorithm utilizes both visible and infrared bands. Mean cloudiness per image is 81.65% for the year, with a maximum occurring in August for both day and night images. Upwelling of deeper, colder ocean water caused by seasonal winds often reach a peak in August. The colder water close to shore provides conditions favorable for fog bank formation.

C. INCLUSION OF CURRENT DATA IN SST MODEL

As part of the California Ocean Currents Monitoring Program (COCMP), multiple land-based high-frequency (HF) radar sites have been installed along the California coast. These sites form a sensor network designed to provide a continuous measurement (in space and time) of coastal surface ocean currents. The presence of clouds do not affect the radar's ability to measure ocean currents. We hypothesize that the inclusion of surface ocean current data will improve existing satellite based SST products whose measurements are hampered by the presence of clouds and fog banks.

The surface current velocity field contains information relevant to the SST field. If, for example, the present SST field is unknown due to clouds, the SST field might be predicted by using a past SST field obtained from some satellite pass in the past when the sky was clear and the surface current velocity data between the time of the past measurement and the current time. For example, if there was a strong

northward current running along the coast, we might expect the surface temperature at a given location to look like the past surface temperature at some point to the south. Figure 2 shows an example of the SST and current fields for Monterey Bay. Notice the stronger westward currents off Point Pinos (at the southern boundary of Monterey Bay) are advecting a cold-water filament into the warmer offshore water mass.

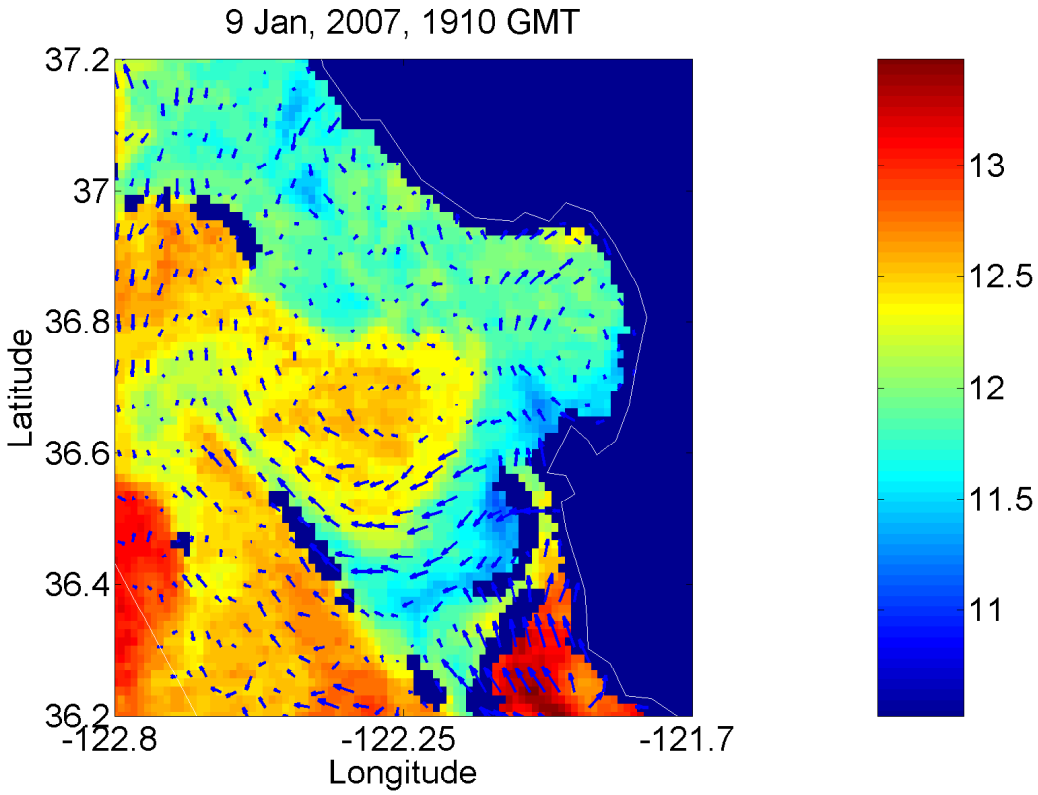

Figure 2. SST (in degrees Celsius) and current field in the Monterey Bay on 19:10 GMT, January 9, 2007.

D. THESIS OBJECTIVES

The main objective of this thesis is to determine if the inclusion of ocean surface current data increases the ability to estimate sea surface temperature in the

presence of clouds. This hypothesis is tested by building a model of SST that advects, or moves, parcels of surface water according to the surface currents measured by the radars. The tracks of these parcels of surface water are called particle trajectories. Particle trajectories are calculated according to the ordinary differential equation,

$$\frac{d\boldsymbol{x}}{dt} = \boldsymbol{u}(t, \boldsymbol{x}(t)), \tag{I.1}$$

where $\boldsymbol{x}(t)$ is the position vector of the particle composed of latitude and longitude components, and $\boldsymbol{u}(t, \boldsymbol{x}(t))$ is the velocity vector composed of latitudinal and longitudinal velocities.

In the particle trajectories, the initial time and location of a particle are called the departure time and departure point, and the final time and location of a particle are called the arrival time and arrival point. In the model, SST at the arrival point at the arrival time is approximated by the SST of a water parcel which has been advected from the departure point at the departure time. To validate the model, SST at the arrival points and arrival times are compared against SST at the departure points and departure times. Note that, in testing the model, the departure and arrival times correspond to the times of satellite passes to allow for new measurements of the SST field. Mathematically, the comparison is expressed as:

$$D = \boldsymbol{T}(t_0, x_0, y_0) - \boldsymbol{T}(t_1, x_1, y_1) \tag{I.2}$$

where $\boldsymbol{T}$, the surface temperature, is a function of time and location (in latitude/longitude coordinates). In this comparison equation, the parcel of water at the departure point (x_0, y_0) at the departure time t_0 is advected by the surface currents to the arrival point (x_1, y_1) at the arrival time t_1. If the advected water parcels temperature is a good prediction of the temperature at the new time and location, then this difference equation should be close to zero.

As a secondary thesis objective, the different methods of calculating ocean currents and particle trajectories are also examined. The two primary methods of

calculating surface currents are compared to each other and to an analytic solution to the Stommel ocean model (discussed in chapter III, section C).

This thesis is divided into four chapters. Chapter I presents a brief background on the thesis investigation. Chapter II discusses the theory behind the thesis material. Chapter III discusses the methods used in calculations and model validation. Chapter IV discusses the results of the model validation and suggests areas of further research.

II. THEORY

A. SST MODEL

As mentioned above, it is proposed that a good predictor of SST is a model that includes both past data about the SST as well as data about the surface current field. In reality, the surface SST field is much more complicated and will depend on additional factors such as surface warming or cooling, mixing with surrounding water masses (through diffusion or turbulent mixing), and horizontal divergence in response to three-dimensional currents (such as upwelling) about which information is not known. While the influence of these processes is acknowledged, they are ignored in this investigation. The model being investigated is the one in which horizontal advection dominates such that a past SST field and surface current data can be used to estimate a present SST field.

When comparing SST measurements to validate the model, both absolute SST and SST anomalies are compared. SST anomalies are defined as

$$SST_a = T(t_j, x_i, y_i) - \left(\frac{\sum_{i=1}^{N} T(t_j, x_i, y_i)}{N} \right), \tag{II.1}$$

where N is the total number of SST measurements in the domain. That is, the anomaly is the difference between the SST measurement at some point and the average SST of the region. By using SST anomalies, it is hoped that some of the influence of large scale warming or cooling is removed. That is, the regional change in time of temperature ($\frac{\partial \boldsymbol{T_{region}}}{\partial t}$) due to energy flux such as warming by the sun is accounted for by only looking at the difference between the local point temperature and the average of temperature over the region. If the entire region's SST is changed by the same amount throughout, then the SST anomaly at any point within the domain will

be unchanged. It is assumed that warming or cooling will occur somewhat uniformly over the region. Localized warming or cooling will produce changes in the anomalies.

B. DESCRIPTION OF HF RADAR

The COCMP seeks to monitor ocean currents off the California coast. Applications of surface ocean currents include, among other uses: search and rescue operations, prediction of chemical and oil spill trajectories, and prediction of trajectories for fish larvae transport.

The primary instrument currently used by COCMP is the Coastal Ocean Dynamics Application (CODAR) High Frequency Radar antennae. These antennas use high frequency electromagnetic pulses to measure ocean currents by a phenomenon known as Bragg scattering along with the Doppler effect [1]. When a pulse of radar energy is sent out, it scatters off the ocean surface in all directions. Some energy is backscattered towards the radar receiver and, of that energy, some is Bragg resonant. The resonant ocean waves are those traveling in a direction either directly towards or directly away from the radar antenna with a wavelength half that of the transmitted radiation. For these ocean waves, the antenna picks up a dramatic spike in returned radiation. This is due to two reasons: the direction of travel of the ocean waves opens up more of the ocean wave face to reflect radiation back towards the radar, and, more importantly, the reflected radiation off one resonant ocean wave is in phase with the reflected radiation off the next resonant ocean wave. This phenomenon is known as Bragg scattering.

From the wavelength of the resonant ocean waves, the theoretical speed of the resonant ocean wave can be calculated from the deep-water dispersion relationship. The deep-water dispersion relationship is:

$$C = \sqrt{\frac{g\lambda}{2\pi}} \tag{II.2}$$

where C is the wave speed, g is the acceleration due to gravity, and λ is the wavelength

of the ocean wave [2]. The wavelength, theoretical speed, and the direction of travel for the Bragg-resonant ocean waves are known. The received signals exhibit a Doppler shift that is slightly different than the shift expected due to the theoretical speed of the ocean waves. In the absence of any other influences, the Doppler shift would always be equal to the speed of the traveling wave. The difference between the theoretical wave speed and the speed measured by Doppler shift is due to ocean currents. Estimates of the uncertainty of radial speed measurements are in the range of 6.9-9.2 cm/sec [3].

Because the radars measure the ocean current speed using a Doppler shift, a single Radar site can only give velocity data for currents moving towards or away from that site. A single radar can only measure the component of current which points towards or away from the radar. Therefore, measurements from multiple sites are needed at any one location to give a complete velocity picture. Figure 3 shows an illustration of how a Total current vector is made from the individual radial components.

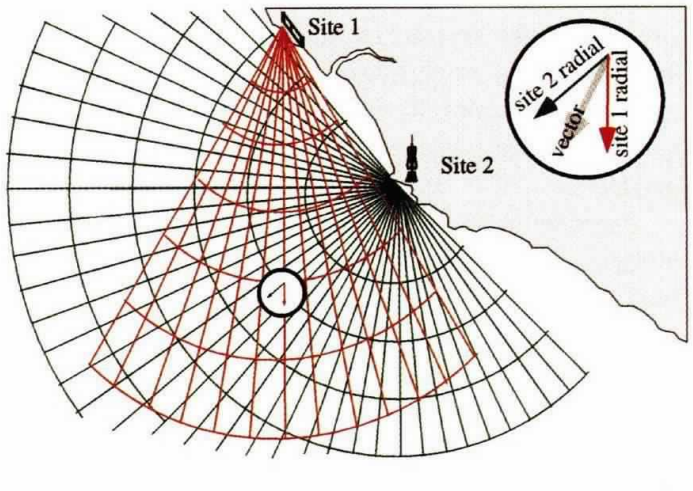

Figure 3. Illustration of Totals method. Figure taken from [1].

The angles between sites should be as close to orthogonal as possible to prevent a problem known as the geometric dilution of precision (GDOP). GDOP occurs when the angles between radar sites are small. Small errors in the radial velocity measurements can lead to large errors in the final current measurement [4]. Figure 4 illustrates the problem that can arise when sites with small separation angles are used to make a total current vector with sampling error. When the measurements are collected without any error, then the resulting current is also without error. But when sampling error is present and the angle spread between sampling sites is small, even small errors (10% in the figure) can lead to large errors in the final current. GDOP is discussed further in later sections.

C. TOTALS SURFACE CURRENT METHOD

The processing of radar measurements to surface current velocities and particle trajectories follows two methods. The first is what will be referred to as the 'Totals method', and the second, the 'Open-boundary Modal Analysis (OMA) method'. Both methods were used to generate currents in this thesis. The resulting currents are compared to each other and to the analytic solution of the Stommel ocean model.

In the processing of radial current measurements to currents by the Totals method, a regular latitude/longitude grid is specified where current measurements are desired. All radial measurements that fall within a specified radius of the grid location are grouped together. A least squares fit is obtained for the total currents at each grid location. The least squares problem is formed as:

$$\boldsymbol{r} = A\boldsymbol{u}. \tag{II.3}$$

If a grid point has n associated radial observations, then $\boldsymbol{r}$ is an nx1 vector of the measured radial velocities, $\boldsymbol{u}$ is a column vector (size 2x1) of the complete

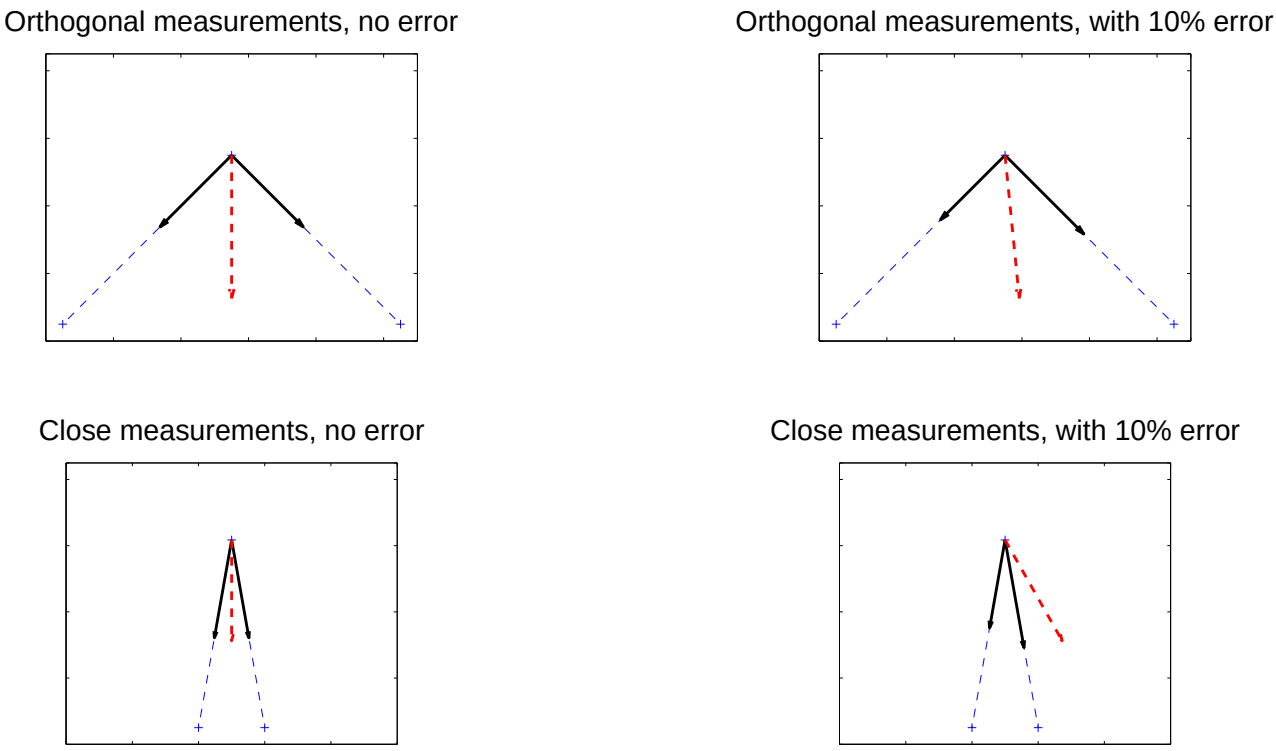

Figure 4. Example of GDOP in radial measurements of a current vector from orthogonal measurement sites (top panes) and measurement sites that are separated by 30° (bottom panes). Black vectors are the radial measurements and red vectors are the resulting total fitted current. In the left panes, radial measurements are sampled without error, and in the right panes radial measurements are sampled with a 10% error.

velocity composed of u and v components, and A is the transformation matrix

$$A = \begin{pmatrix} \cos\theta_1 & \sin\theta_1 \\ \cos\theta_2 & \sin\theta_2 \\ . & . \\ . & . \\ . & . \\ \cos\theta_n & \sin\theta_n \end{pmatrix}, \tag{II.4}$$

where θ_i is the bearing from the i^{th} radial measurement to the radar site that took the measurement [5]. At a minimum, a radial measurement from two different radar sites are needed to generate the total current measurement at a single point. Radial measurements from additional radar sites will provide more information about the currents at the grid point and, in the absence of problems, give a better measurement of the total current. The surface current field, which now contains current measurements at the specified points of the regular grid, may be cleaned by removing currents with unreasonably large surface current magnitudes or with large errors. Figure 5 shows an example one-hour current field of the radar domain off central California. This current field was calculated using the Totals method.

Error measurements are also generated in calculating totals currents. Most error measurements center around the concept of GDOP and are a function of the spread of the angles of radial measurements that make the total current vector. If A is the matrix which is used in the least squares fit of radial measurements to total currents, then the covariance matrix of the total current components u and v is the 2x2 matrix:

$$Cov = \sigma^2 (A^T A)^{-1}, \tag{II.5}$$

where σ^2 is the variance of the radial measurements. The variance of the u and v total velocity components are the first and second diagonal entries of this matrix, respectively. The covariance of u and v are the off-diagonal entries [6]. Notice that as the angles between two radar sites become close to parallel, the matrix $(A^T A)$

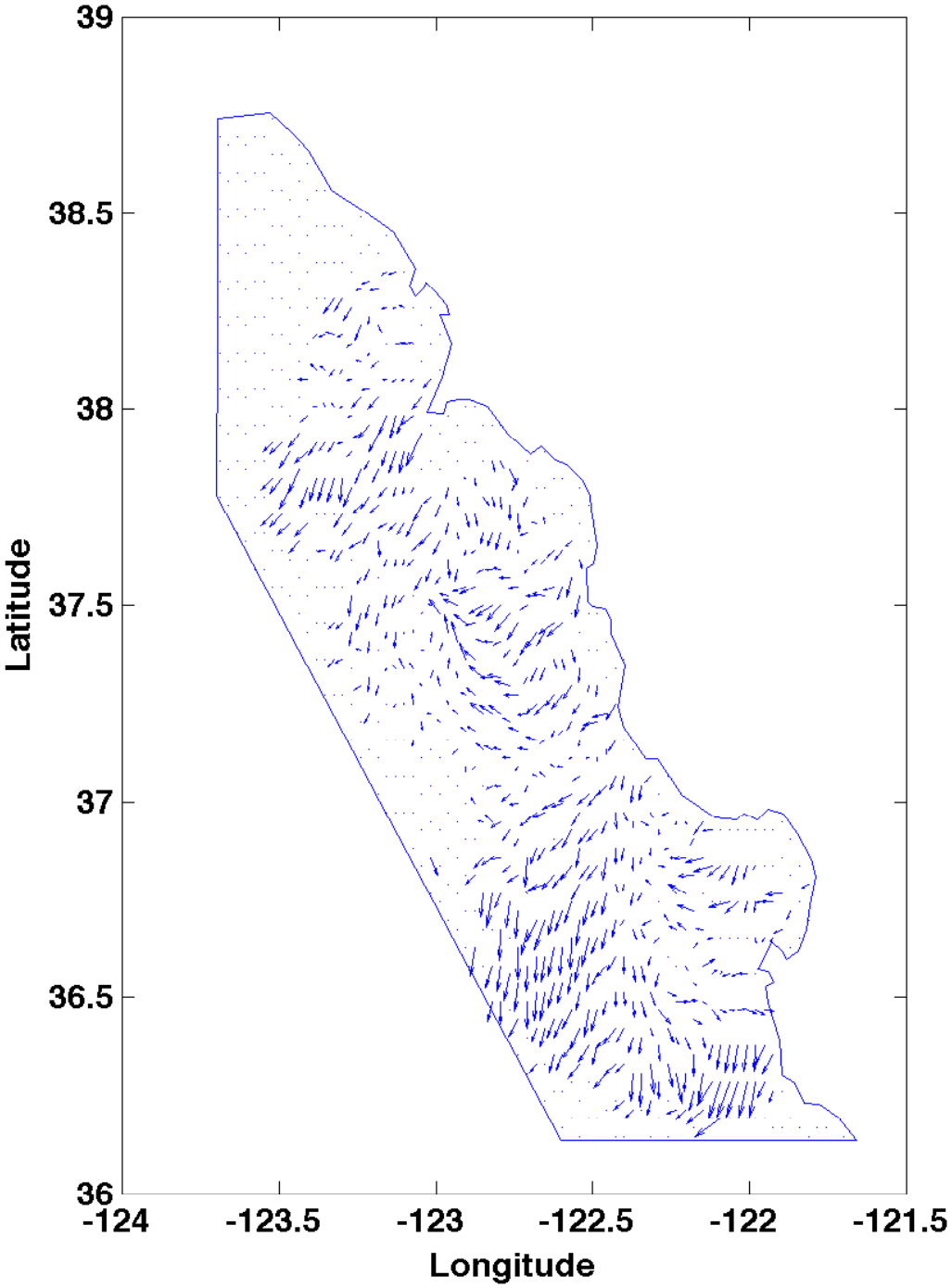

Figure 5. Totals current field for CENC region on 06:00 GMT, 19 October, 2006. Every 4^{th} vector is plotted.

becomes close to singular, and the inverse of $(A^T A)$ contains very large values. For angles which are exactly parallel, the inverse of $(A^T A)$ does not exist. As the angles between two radar sites become close to parallel, *any* sampling error will produce very large variances in the u and v fitted velocities. That is, even if σ^2 is very small, the diagonal elements of equation II.5 will still tend towards infinity for close radar measurements.

A GDOP error estimate is formed by setting a unit radial measurement variance ($\sigma^2 = 1$). With this substitution for σ, the error estimate is purely a measure of the loss of precision due to the angular spread of the radial measurements. If additional information is known about the variance of the radial measurements that makes the total current (σ^2), then that can be added to equation II.5 to produce another type of error measurement.

The covariance matrix is formed as above in equation II.5, and the total GDOP error measurement is defined to be:

$$E = \sqrt{\| \, Cov \, \|}. \tag{II.6}$$

That is, the total GDOP error is the square root of the covariance matrix 2-norm, or the square root of the largest eigenvalue of the covariance matrix. This total GDOP error measurement is a function of angle separation. Figure 6 is a plot of the GDOP against angle separation. The GDOP error function reaches a minimum of one at orthogonal angles (angle separations of 90° or 270°) and tends towards infinity as the angle vectors approach parallel (0° or 180°). This total error is close, but not equal, to the square root of the sum of the squares of the two variances (diagonal elements).

Another error measurement involves finding the GDOP using only the two most-orthogonal radial measurements that make a current vector. This is perhaps more useful than the GDOP calculated with all the radial measurement angles. In the full GDOP error measurement, additional radial measurements with the same angles (additional rows in the A matrix) will lower the GDOP error. The reduction

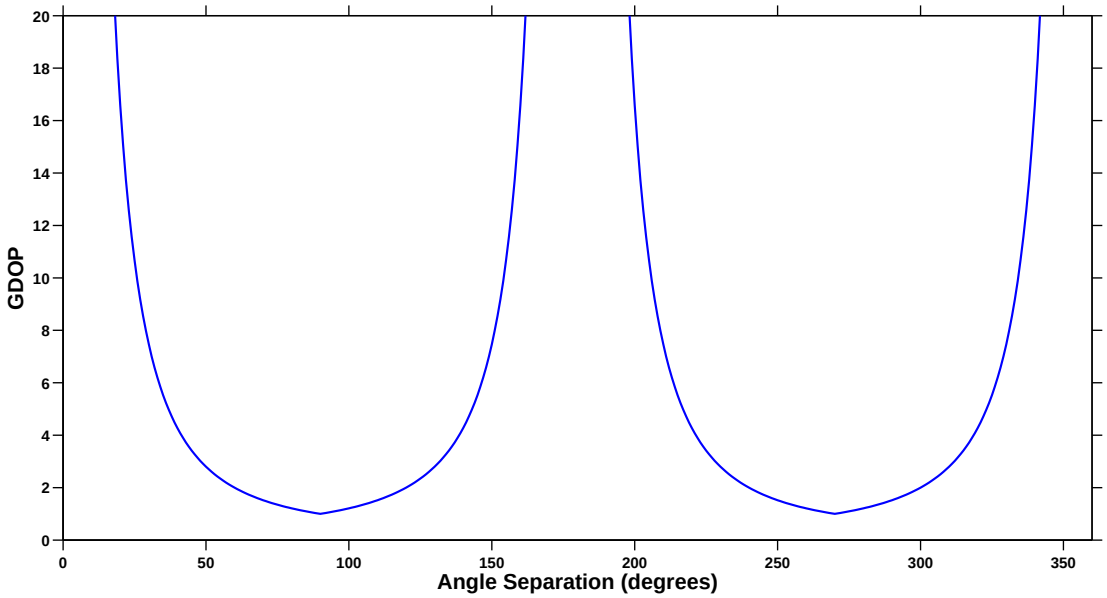

Figure 6. GDOP error as a function of angle separation

in GDOP is somewhat artificial because the additional radial measurements measure the same component of current and add no new information to the least-squares fit.

D. OPEN MODAL ANALYSIS METHOD

The second method of processing radar measurements to the current velocity field uses a method called Open-boundary Modal Analysis, or OMA. The OMA method used in this thesis follows the procedure described in [7]. The general idea of OMA is to generate a set of modes for a given domain which can be used to approximate any current field on that domain. The modal series approximation is determined by minimizing a cost function to find the ideal combination of the modes which gives the best fit to available measurement data. These modes depend only on the shape of the domain. Once they are calculated, they can be stored for repeated use on the same domain.

In OMA, the domain of interest need not be rectangular. Furthermore, the boundary of the domain Ω can be composed of multiple open and closed segments. An open segment is one along which the normal component of the velocity can be nonzero. Vector currents are allowed to flow into or out of an open segment. A closed segment is one in which the normal component of the velocity is fixed at zero and no current is allowed to flow through the segment, although currents can flow parallel to a closed segment.

In theory, the OMA method offers several advantages over the totals currents method. The generation of the OMA modes is only done once. Afterwards, when fitting the currents to the OMA modes, one least-squares matrix equation needs to be solved. This is computationally similar to the problem of finding currents with the totals method. Unlike the totals method however, the modes are defined over the entire domain, even for sparse current measurements. The fit results in a current field which is also defined over the entire domain without gaps. This is a nice feature of the OMA method, but should be utilized with caution. Currents will be reported even in areas with few or no actual measurements. Currents in these areas are an extrapolation of the modal fit to data in other areas, and they do not represent the "real" currents. Attention should be paid to how much real data goes into making the fit.

1. Calculation of Modes

The first step in OMA is to calculate the basis functions (modes) that are later used to reconstruct the current velocities. The modes depend only on the shape of the domain, and the calculation of the modes needs to be done only once for a particular domain. Proceeding as in [7], it is noted that any vector field $\boldsymbol{u}$ on a domain Ω can be decomposed into an irrotational (curl-free) vector component $\boldsymbol{u}_{\boldsymbol{\varphi}}$ and a solenoidal (divergence-free) vector component $\boldsymbol{u}_{\boldsymbol{\psi}}$. This decomposition is known as Helmholtz's Theorem, or the Fundamental Theorem of Vector Analysis, and is written as:

$$\boldsymbol{u} = \boldsymbol{u}_{\boldsymbol{\varphi}} + \boldsymbol{u}_{\boldsymbol{\psi}}. \tag{II.7}$$

Because $\boldsymbol{u_\varphi}$ is curl-free, or irrotational, it is a conservative field and there exists a scalar potential function φ such that:

$$\boldsymbol{u_\varphi} = \boldsymbol{\nabla}\varphi. \tag{II.8}$$

The field $\boldsymbol{u_\psi}$ is divergence-free, or solenoidal, and can be expressed in terms of a stream function ψ:

$$\boldsymbol{u_\psi} = \hat{\boldsymbol{k}} \times \boldsymbol{\nabla}\psi, \tag{II.9}$$

where $\hat{\boldsymbol{k}}$ is the unit vector pointing out of the plane.

It can be verified that $\boldsymbol{u_\varphi}$ is curl-free and $\boldsymbol{u_\psi}$ is divergence-free. By taking the divergence of $\boldsymbol{u}$, the following nonhomogeneous partial differential equation results for φ:

$$\boldsymbol{\nabla}\cdot\boldsymbol{u} = \boldsymbol{\nabla}\cdot(\boldsymbol{u_\varphi} + \boldsymbol{u_\psi}) = \boldsymbol{\nabla}\cdot\boldsymbol{u_\varphi} + \boldsymbol{\nabla}\cdot\boldsymbol{u_\psi} = \boldsymbol{\nabla}\cdot\boldsymbol{\nabla}\varphi = (\frac{\partial}{\partial x}\hat{\boldsymbol{i}} + \frac{\partial}{\partial y}\hat{\boldsymbol{j}})\cdot(\frac{\partial\varphi}{\partial x}\hat{\boldsymbol{i}} + \frac{\partial\varphi}{\partial y}\hat{\boldsymbol{j}}) = \boldsymbol{\nabla}^2\varphi. \tag{II.10}$$

By taking the curl of $\boldsymbol{u}$, the following nonhomogeneous PDE results:

$$\boldsymbol{\nabla}\times\boldsymbol{u} = \boldsymbol{\nabla}\times(\boldsymbol{u_\varphi} + \boldsymbol{u_\psi}) = \boldsymbol{\nabla}\times(\hat{k}\times\boldsymbol{\nabla}\psi) = \boldsymbol{\nabla}\times(-\frac{\partial\psi}{\partial y}\hat{\boldsymbol{i}} + \frac{\partial\psi}{\partial x}\hat{\boldsymbol{j}}) = \boldsymbol{\nabla}^2\psi\hat{\boldsymbol{k}}. \tag{II.11}$$

Taking the dot product of equation II.11 and $\hat{\boldsymbol{k}}$ gives

$$\hat{\boldsymbol{k}}\cdot(\boldsymbol{\nabla}\times\boldsymbol{u}) = \boldsymbol{\nabla}^2\psi. \tag{II.12}$$

a. Interior Modes

This formulation for φ and ψ is not unique. For example, φ and ψ plus any constant still satisfy equations II.10 and II.12. Hence there is some degree of freedom and some flexibility on the choice of boundary conditions along $\mathrm{d}\Omega$, the boundary of the domain Ω. The authors of [7] chose to define ψ to be zero along the entire boundary, and specify the normal component of the flow of $\boldsymbol{u}$ solely in terms of φ. To solve this pair of equations (II.10 and II.12), the method of eigenfunction

expansion is used. φ and ψ are expanded in terms of their eigenfunctions, hereafter called modes, which are solutions to:

$$\boldsymbol{\nabla}^2\psi_i = \lambda_i\psi_i, \qquad \psi_i|_{d\Omega} = 0 \tag{II.13}$$

$$\boldsymbol{\nabla}^2\varphi_i = \lambda_i\varphi_i, \quad (\hat{\boldsymbol{n}}\cdot\boldsymbol{\nabla}\varphi_i)|_{d\Omega} = 0. \tag{II.14}$$

Because of the specific boundary conditions imposed on φ and ψ, the eigenmodes of φ are called Neumann modes and the eigenmodes of ψ are called Dirichlet modes. Equations II.13 and II.14 are two Sturm-Liouville equations, and ϕ_i and φ_i are eigenfunctions of the Sturm-Liouville equations. They are linearly independent and form a basis for the space of solutions of the Sturm-Liouville problem. As a result, the vector fields $\boldsymbol{\nabla}\varphi_i$ and $\hat{k}\times\boldsymbol{\nabla}\psi_i$ reconstructed from the modes φ_i and ψ_i form a basis for all two dimensional vector fields in Ω [8]. The series of eigenmodes of φ and ψ are used to reconstruct a velocity field $\boldsymbol{u}$ as:

$$\boldsymbol{u} = \sum_{i=1}^{\infty}\alpha_i^{\psi}(\hat{\boldsymbol{k}}\times\boldsymbol{\nabla}\psi_i) + \sum_{i=1}^{\infty}\alpha_i^{\varphi}\boldsymbol{\nabla}\varphi_i, \tag{II.15}$$

where the α_i are unknown coefficients.

The important limitation so far being that any combination of the currents reconstructed from φ and ψ will have zero flow on the domain boundary $d\Omega$. This is verified by checking the normal component of the current associated with each mode, $\hat{\boldsymbol{n}}\cdot\boldsymbol{u}$, on the boundary.

$$\hat{\boldsymbol{n}}\cdot\boldsymbol{u}_{\boldsymbol{\varphi}} = \hat{\boldsymbol{n}}\cdot\boldsymbol{\nabla}\varphi_i = 0, \tag{II.16}$$

due to the boundary conditions of equation II.14. Also,

$$\hat{\boldsymbol{n}}\cdot\boldsymbol{u}_{\boldsymbol{\psi}} = \hat{\boldsymbol{n}}\cdot(\hat{\boldsymbol{k}}\times\boldsymbol{\nabla}\psi_i) = \hat{\boldsymbol{n}}\cdot(-\frac{\partial\psi}{\partial y}\hat{\boldsymbol{i}} + \frac{\partial\psi}{\partial x}\hat{\boldsymbol{j}}). \tag{II.17}$$

To verify that this is zero on the domain boundary, let $\hat{\boldsymbol{t}}$ be a unit vector tangent to the domain boundary. Because $\psi_i|_{d\Omega} = 0$, the boundary is a contour line in ψ, and $\boldsymbol{\nabla}\psi$ is necessarily orthogonal to the boundary and $\hat{\boldsymbol{t}}$. If $\hat{\boldsymbol{t}}$ is composed of vector

components, $(x_t\hat{\boldsymbol{i}} + y_t\hat{\boldsymbol{j}})$, then

$$\hat{\boldsymbol{t}} \cdot \boldsymbol{\nabla}\psi_i = (x_t\hat{\boldsymbol{i}} + y_t\hat{\boldsymbol{j}}) \cdot \boldsymbol{\nabla}\psi_i = (x_t\hat{\boldsymbol{i}} + y_t\hat{\boldsymbol{j}}) \cdot (\frac{\partial\psi}{\partial x}\hat{\boldsymbol{i}} + \frac{\partial\psi}{\partial y}\hat{\boldsymbol{j}}) = x_t\frac{\partial\psi}{\partial x} + y_t\frac{\partial\psi}{\partial y} = 0, \quad \text{(II.18)}$$

which implies

$$x_t\frac{\partial\psi}{\partial x} = -y_t\frac{\partial\psi}{\partial y}. \quad \text{(II.19)}$$

Combining this with equation II.17 and the specification that $\hat{\boldsymbol{t}} = \hat{\boldsymbol{n}} \times \hat{\boldsymbol{k}}$, gives $\hat{\boldsymbol{n}} = (-y_t\hat{\boldsymbol{i}} + x_t\hat{\boldsymbol{j}})$ (due to the orthogonality of $\hat{\boldsymbol{n}}$ and $\hat{\boldsymbol{t}}$). Thus,

$$\hat{\boldsymbol{n}} \cdot \boldsymbol{u}_{\boldsymbol{\psi}} = (-y_t\hat{\boldsymbol{i}} + x_t\hat{\boldsymbol{j}}) \cdot (-\frac{\partial\psi}{\partial y}\hat{\boldsymbol{i}} + \frac{\partial\psi}{\partial x}\hat{\boldsymbol{j}}) = y_t\frac{\partial\psi}{\partial y} + x_t\frac{\partial\psi}{\partial x} = -x_t\frac{\partial\psi}{\partial x} + x_t\frac{\partial\psi}{\partial x} = 0. \quad \text{(II.20)}$$

And so it is shown that the normal component of the current associated with ψ_i along the domain boundary is also zero.

b. Boundary Modes

Since an arbitrary domain will consist of both closed and open boundary segments, the full reconstruction of a current field must include flow across open boundary segments. Open boundary flow is accounted for by including a set of boundary modes, φ_i^b. These boundary modes satisfy:

$$\boldsymbol{\nabla}^2\varphi^b|_\Omega = \frac{1}{A}\oint_{d\Omega} g(s)ds, \quad \text{(II.21)}$$

$$\left(\hat{n} \cdot \boldsymbol{\nabla}\varphi^b\right)|_{d\Omega} = \hat{n} \cdot \boldsymbol{u}^b|_{d\Omega} = g(s), \quad \text{(II.22)}$$

$$\int\int_\Omega \varphi^b dA = 0, \quad \text{(II.23)}$$

where A is the total area of the domain Ω and $g(s)$ is some function of the distance along the domain boundary. Equation II.21 results from the Divergence Theorem, which states that the volume integral of the divergence of a vector field is equal to the flux of the vector field through the surface of the volume. The two-dimensional analog is that the surface integral of the divergence of a surface vector field is equal to the flux of the vector field through the boundary. In mathematical language,

$$\int\int_\Omega \boldsymbol{\nabla} \cdot \boldsymbol{u}\ dA = \int_{d\Omega} \boldsymbol{u} \cdot \hat{\boldsymbol{n}}\ ds. \quad \text{(II.24)}$$

Combining equation II.24 with II.10 gives:

$$\int\int_{\Omega} \boldsymbol{\nabla} \cdot \boldsymbol{u} \; dA = \int\int_{\Omega} \boldsymbol{\nabla}^2 \varphi \; dA = \int_{d\Omega} \boldsymbol{u} \cdot \hat{\boldsymbol{n}} \; ds = \int_{d\Omega} g(s) \; ds. \tag{II.25}$$

The left-hand side of equation II.21 represents the average of the Laplacian of φ^b over the domain. Notice that the interior modes of φ satisfy equation II.14, while the boundary modes of φ are allowed to have flow through the boundary ($\hat{\boldsymbol{n}} \cdot \boldsymbol{\nabla} \varphi^b \neq 0$). The normal flow across open boundary segments, $\hat{\boldsymbol{n}} \cdot \boldsymbol{u}|_{d\Omega}$, is given by measured data, if available. Other data, such as current data from numerical models, may also be used to specify normal boundary flow. To solve equations II.21 - II.23, the boundary function $g(s)$ is expanded in terms of a set of basis functions. Any set of basis functions can be used, though one convenient set is the set of Fourier basis functions $g_i(s) = \{\cos \frac{2\pi i s}{l}, \sin \frac{2\pi i s}{l}\}$, where, again, s is the distance along the domain boundary, l is the total length of the boundary, and i is a basis index. The boundary mode process is similar to solving a nonhomogeneous ODE, whereby the solution to the homogeneous problem is found first, and then a particular solution to the nonhomogeneous problem is found. In the case of OMA, the interior modes satisfy the homogeneous problem (with no boundary flow), and the boundary modes satisfy the nonhomogeneous problem (with boundary flow specified by measured data). By the principle of superposition, the sum of the general solution and the particular solution is also a solution. More information on the boundary modes is available in [7] and [8].

With these boundary modes added, the full current field (including current through open boundary segments) is reconstructed as:

$$\boldsymbol{u} = \sum_{i=1}^{\infty} \alpha_i^{\psi} (\hat{\boldsymbol{k}} \times \boldsymbol{\nabla} \psi_i) + \sum_{i=1}^{\infty} \alpha_i^{\varphi} \boldsymbol{\nabla} \varphi_i + \sum_{i=1}^{\infty} \alpha_i^{b} \boldsymbol{\nabla} \varphi_i^b. \tag{II.26}$$

Since the exact solution of the PDE will involve an infinite number of modes, some stopping criteria is specified in the mode generation. This is done by specifying a mode scale. All modes on a scale less than the stopping scale are thrown out. More detail on the scale and stopping criteria is contained in [7].

2. Unstructered Grid

In contrast to the total currents method, the OMA method is not calculated on a rectangular grid. The PDE is instead solved on an unstructured triangular mesh. Rectangular grids can be problematic for solving PDEs on arbitrary non-rectangular domains. If greater grid resolution is desired (along a coastline for example), a rectangular mesh must be subdivided across the entire domain, leading to vast increases in processing time and required resources. Furthermore, a complex coastline approximated by rectangles might have problems if a no-flow boundary condition is applied on the artificial 'corners' of the coast. It should be noted that in our case, no no-flow boundary conditions were applied in the rectangular grid (totals method). In that case, the currents were generated from a least-squares fit to the radial measurements, and any current vectors falling on the coastline (from erroneous radial measurements, for example) were masked out. Currents next to the coastline, however, are allowed to have current vectors that appear to flow through the coastline. Figure 7 shows an example of a grid mesh and an unstructured triangular mesh applied near a coastline point.

With an unstructured triangular mesh, however, higher resolution is available in the areas where it is needed without unecessarily increasing resolution across the entire domain. In addition, no-flow boundary conditions can be applied in a more realistic manner.

3. Fitting Current Data to OMA Modes

Once the modes are calculated, any current field (up to the scale of modes that were kept) can be represented as a linear combination of these modes. The linear combination is written in equation II.26. The coefficients of the modes in this linear combination are found by fitting the existing current measurements to the OMA modes. The currents are fit using the u and v components of the total currents generated from the radial measurements or using the radial measurements directly. Using radial measurements directly to find the OMA mode coefficients is generally

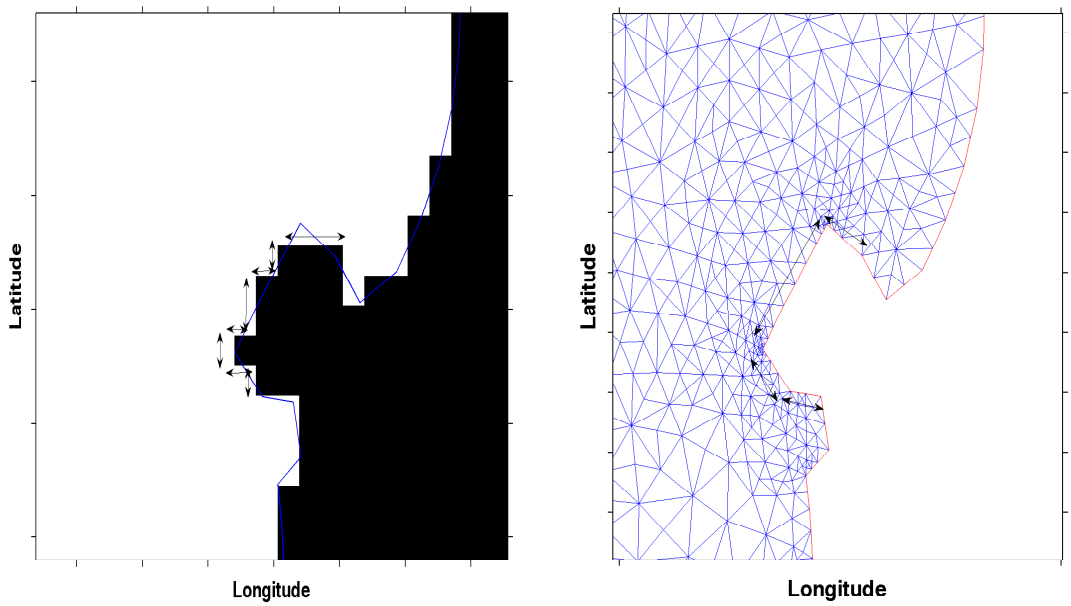

(*a*) (*b*)

Figure 7. Example of Coastline Grid around Point Pinos at the souther end of Monterey Bay using (*a*) Rectangular Grid, and (*b*) Unstructured Triangular Mesh. Both panes show the flow conditions on the domain boundary. Arrows indicate allowed direction of allowed flow.

preferable because it avoids the additional error introduced during the radials to totals calculation. In fitting the modes to existing current data, the mode coefficients are calculated that provide the minimal error between modal currents and currents measured by radar. This is done by minimizing a cost function. The cost function is defined as the square root of the sum of the squared differences between modal currents and measured currents, although other cost functions could be used. One adjustment to the cost function used in the processing of this thesis is to add a penalty for large mode coefficients. This prevents modal currents from becoming unrealistically large in areas where there are no current measurements to constrain them. In areas where measured data is sparse, modal currents can become quite large without affecting the difference between modal currents and measured currents. The

large coefficient penalty term in the cost function reduces the tendency of the fitted currents to become unreasonably large in areas where data measurements are sparse. Additionally, weights may be introduced to place more importance on certain data, although this is not done in this thesis.

The general cost function used to find mode coefficients is:

$$\zeta = \sqrt{\sum_{m=1}^{M}\left[W_m^r\left(\sum_{n=1}^{N}(\alpha_n \boldsymbol{u_n}(x_m))\cdot\hat{\boldsymbol{r}}_{\boldsymbol{m}} - u_m^r\right)^2\right] + \frac{M}{2}\sum_{n=1}^{N}\kappa_n\alpha_n^2}, \tag{II.27}$$

where M is the total number of measurements, N is the total number of modes, $\boldsymbol{u_n}(x_m)$ is the current at location m associated with the n^{th} mode, $\hat{\boldsymbol{r}}$ is the unit vector from the current location to the radar site, and u_m^r is the measured radial current at location m in the direction of $\hat{\boldsymbol{r}}$. To minimize this function, note that minimizing the square of this cost function is equivalent to minimizing the cost function itself. Taking $\frac{\partial(\zeta^2)}{\partial\alpha_n}$ and setting equal to zero gives

$$\frac{\partial(\zeta^2)}{\partial\alpha_n} = \sum_{m=1}^{M}\left[2W_m^r\left(\sum_{n=1}^{N}(\alpha_n\boldsymbol{u_n}(x_m))\cdot\hat{\boldsymbol{r}}_{\boldsymbol{m}} - u_m^r\right)(\boldsymbol{u_j}(x_m)\cdot\hat{\boldsymbol{r}}_{\boldsymbol{m}})\right] + M\kappa_j\alpha_j = 0 \tag{II.28}$$

for all coefficients α_j. This is a linear set of M equations in N unknowns. The system can be solved exactly if N measurements exist ($M = N$), or can be approximated with a least squares solution if more than N measurements exist ($M > N$). An overdetermined system is preferable to an exact solution, since the measurements contain noise which can presumably be filtered out if many more measurements than modes exist ($M \gg N$).

To ensure that equation II.28 is indeed a minimum of the cost function equation II.27, the second derivative is examined.

$$\frac{\partial(\zeta^2)^2}{\partial\alpha_n^2} = \sum_{m=1}^{M}\left[2W_m^r(\boldsymbol{u_j}(x_m)\cdot\hat{\boldsymbol{r}}_{\boldsymbol{m}})^2\right] + M\kappa_j \tag{II.29}$$

Assuming that the large coefficient penalty, κ, and the weights, W_m^r are both positive, equation II.29 is everywhere positive and equation II.28 is guaranteed to be a minimum of the cost function II.27.

E. PARTICLE TRAJECTORIES

Once the current field is known, forward particle trajectories can be calculated. A particle trajectory describes the path a particle takes when moving with a velocity described by the current velocity field. The trajectories are calculated by solving the ordinary differential equation (ODE):

$$\frac{d\boldsymbol{x}}{dt} = \boldsymbol{u}(t, \boldsymbol{x}(t)), \tag{II.30}$$

where $\boldsymbol{x}$ is the position vector composed of latitude and longitude coordinates and $\boldsymbol{u}(t, \boldsymbol{x}(t))$ is the velocity vector composed of latitudinal and longitudinal velocities.

Many techniques are available for numerical solution of ODEs. The trajectory equation II.30 is solved using the Runge-Kutta fourth-order, fifth-stage method during this investigation. The Runge-Kutta fourth-order, fifth-stage method for solving ordinary differential equations is a one-step, multi-stage method. It is a one-step method in that to find the value of $\boldsymbol{x}(t_{i+1})$, only data from the previous point $\boldsymbol{x}(t_i)$ is used. The Runge-Kutta fourth-order, fifth-stage method uses the following scheme: let $\frac{dy}{dt} = f(t, y)$ be an ordinary differential equation with initial condition $y(t_0) = y_0$. The solution to this initial value problem can be approximated numerically by:

$$y_{n+1} = y_n + h(b_1k_1 + b_2k_2 + b_3k_3 + b_4k_4 + b_5k_5), \tag{II.31}$$

where

$$k_1 = f(t_n, y_n) \tag{II.32}$$

$$k_2 = f(t_n + c_2h, y_n + h(a_{21}k_1)) \tag{II.33}$$

$$k_3 = f(t_n + c_3h, y_n + h(a_{31}k_1 + a_{32}k_2)) \tag{II.34}$$

$$k_4 = f(t_n + c_4h, y_n + h(a_{41}k_1 + a_{42}k_2 + a_{43}k_3)) \tag{II.35}$$

$$k_5 = f(t_n + c_5h, y_n + h(a_{51}k_1 + a_{52}k_2 + a_{53}k_3 + a_{54}k_4)). \tag{II.36}$$

The coefficients a_i, b_i, c_i are given by the particular fourth-order Runge-Kutta algorithm being used and h is the step size. The fifth stage is used to bound the

error of the approximation y_{n+1}. The error can be controlled by examining the fifth stage and varying the step size h to keep the local truncation error below a specified bound.

In the case of this thesis, equation II.30 is the ODE that is solved to make particle trajectories. Let $\boldsymbol{x}_n$ be the particle position at time t_n. Then the particle position at the next time step t_{n+1} is approximated by:

$$\boldsymbol{x}_{n+1} = \boldsymbol{x}_n + h(b_1k_1 + b_2k_2 + b_3k_3 + b_4k_4 + b_5k_5), \tag{II.37}$$

where

$$k_1 = \boldsymbol{u}(t_n, \boldsymbol{x}_n) \tag{II.38}$$

$$k_2 = \boldsymbol{u}(t_n + c_2h, \boldsymbol{x}_n + h(a_{21}k_1)) \tag{II.39}$$

$$k_3 = \boldsymbol{u}(t_n + c_3h, \boldsymbol{x}_n + h(a_{31}k_1 + a_{32}k_2)) \tag{II.40}$$

$$k_4 = \boldsymbol{u}(t_n + c_4h, \boldsymbol{x}_n + h(a_{41}k_1 + a_{42}k_2 + a_{43}k_3)) \tag{II.41}$$

$$k_5 = \boldsymbol{u}(t_n + c_5h, \boldsymbol{x}_n + h(a_{51}k_1 + a_{52}k_2 + a_{53}k_3 + a_{54}k_4)). \tag{II.42}$$

$\boldsymbol{u}$(t,$\boldsymbol{x}$(t)) is the current velocity field.

In the numerical solution of many ODEs, evaluations of the function $\frac{dy}{dt} = f(t, y)$ are a computational expensive step. In this thesis, evaluating the derivative of the position vector simply involves a lookup in the velocity data field, which contains velocity information at specific grid points. When the value of the derivative is needed at a location not specified in the current fields (any location other than the grid points), interpolation is done to approximate the currents at the desired points. If the current field is the output of the totals current method, then the field is defined on a regular latitude/longitude grid. Simple bilinear interpolation in space is used to interpolate between the nearest four latitude/longitude points where the currents are known. If the current field is the output of the OMA method, then the currents are defined on a triangular mesh. Currents are assumed to be constant across a triangle, and if a current measurement is needed at a grid point that is not the center of a

triangle, then the current value for whatever triangle the grid point falls within is returned. This is nearest neighbor interpolation. For both the Totals method and the OMA method, bilinear interpolation in time is performed last to find current values at times not specified in the current field.

Bilinear interpolation is not a highly accurate interpolation scheme. Higher order interpolation methods are available that give greater accuracy in interpolating functions. However, the sampling error inherent in the current fields (error on the order of 10%) usually will dominate any error resulting from interpolation, making higher order interpolation methods unnecessary [3].

III. METHODS

A. MODEL VALIDATION AND SST COMPARISONS

Figure 8 shows a flow chart of the processing and validation procedure. The SST comparisons formed the main test of the thesis hypothesis. SST was compared in three different ways: advected SST comparison, static SST comparison, and random SST comparison. The advected method of SST comparison compared SST according to the hypothesized model. Static and random comparison methods were meant as baselines. In each case, absolute SST and SST anomaly were used in the comparison.

Statistics were calculated on the SST differences between all the points in the comparison. One statistic used in the comparisons is the root mean square (RMS) difference. The RMS is defined as:

$$RMS_{difference} = \sqrt{\frac{\sum_{k=1}^{n} (\boldsymbol{T_k}(t_0, x_0, y_0) - \boldsymbol{T_k}(t_1, x_1, y_1))^2}{n}}. \tag{III.1}$$

That is, the RMS difference is the square root of the average of the squared temperature differences.

In the advected method, SST values at the arrival points are compared with SST values at the departure points. Between images, many points are compared. An illustration of the advected comparison is shown in Figure 9.

In the static comparison method, SST values at the arrival points in the second image were compared against SST values *at those same locations* in the first image. Again, statistics were calculated on the SST differences of all the points in the comparison. An illustration of the static comparison method is shown in Figure 10.

In the random comparison method, SST values at the arrival points in the second image were compared against random points *within the same image*. An illustration of the random comparison method is shown in Figure 11.

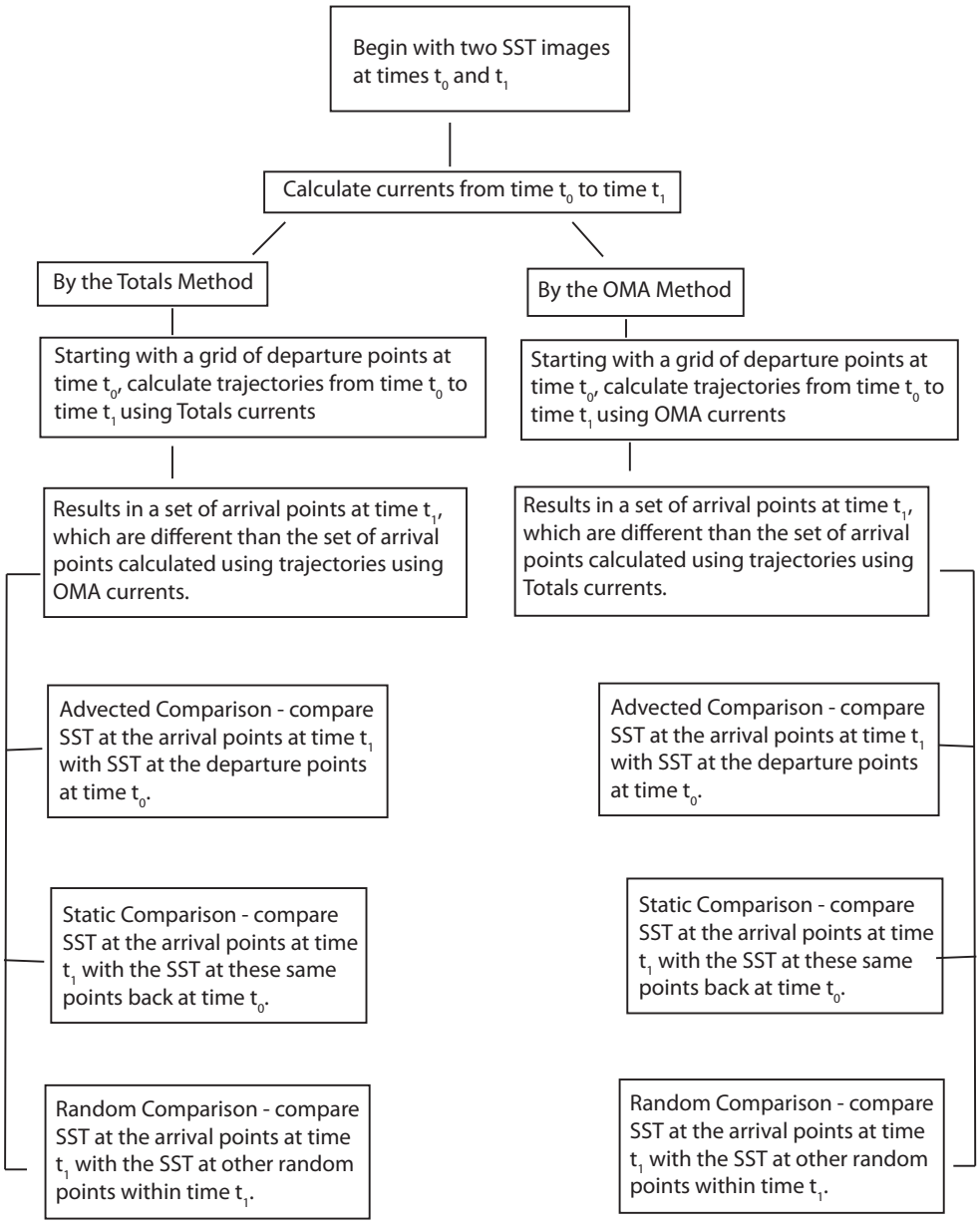

Figure 8. Flow chart of SST comparison procedure.

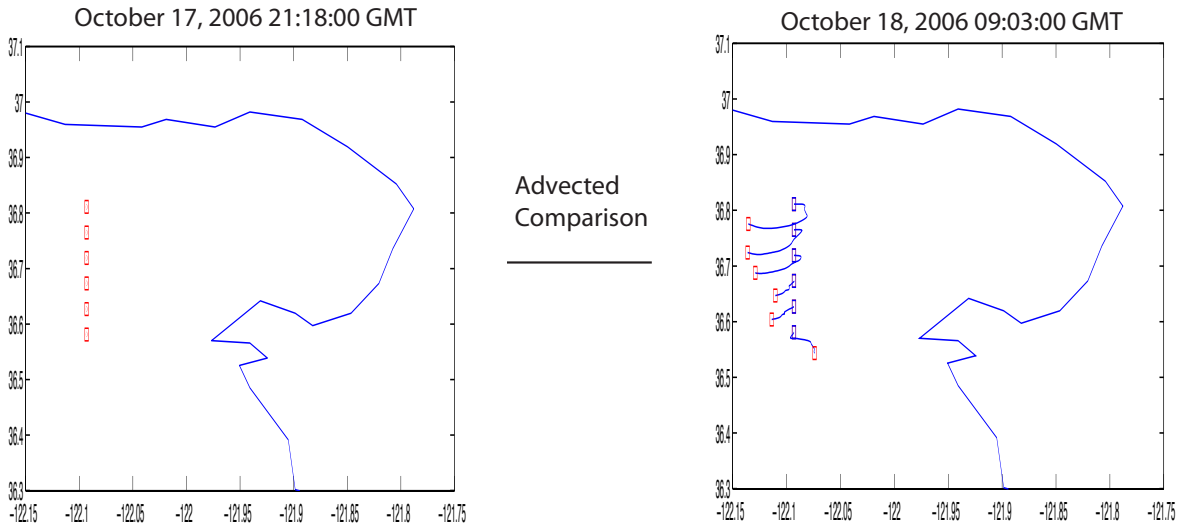

Figure 9. Example illustration of comparison of advected points between SST images.

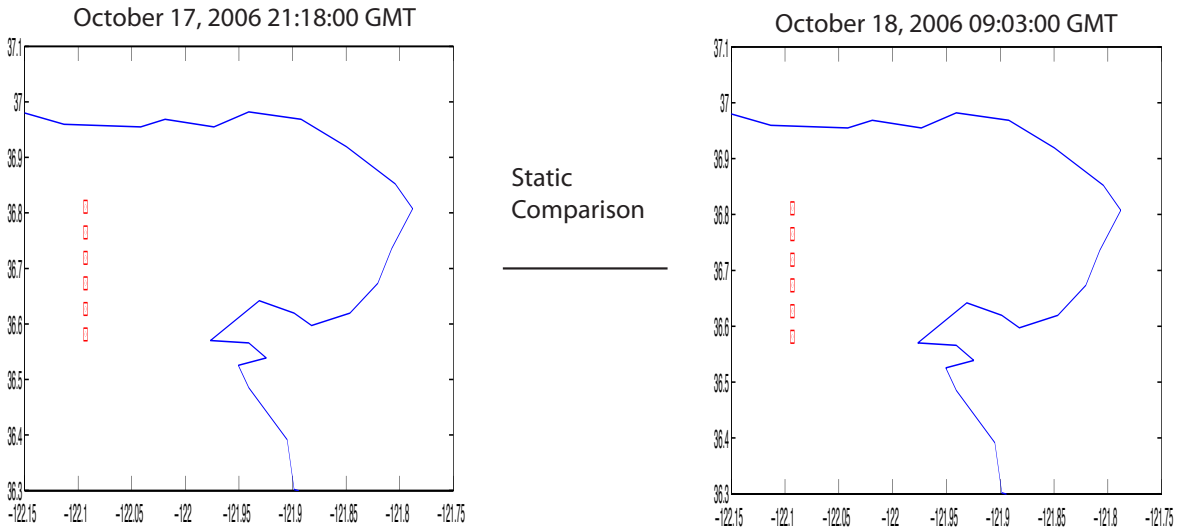

Figure 10. Example illustration of static comparison of points between SST images.

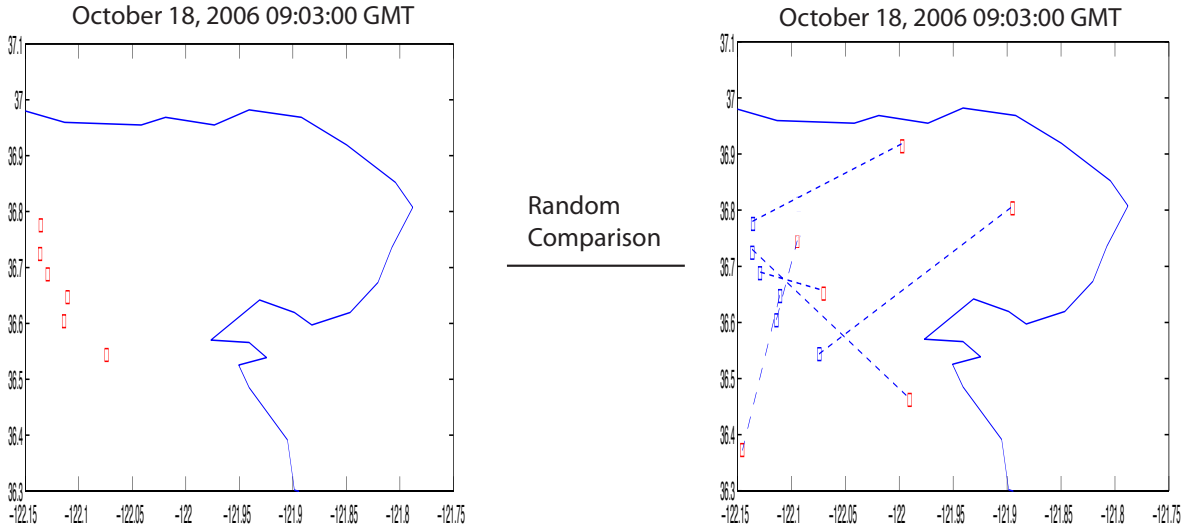

Figure 11. Example illustration of comparison of random points within a SST images.

In testing the hypothesized model, all possible combinations of SST images within the case study are compared with each other. Each comparison method (advected, static, and random) was used in the comparison between each pair of images. If the advected method is a good predictor of SST, then the RMS statistic of the advected comparisons will be closer to zero than the RMS statistic of the other comparison methods.

B. DATA USED

1. SST Data

As mentioned previously, we used the NOAA high resolution AVHRR SST dataset in this thesis. All single-pass POES SST images were downloaded for the case study periods at the highest resolution available, approximately 1.5km. Data from each satellite pass within the case-study periods were downloaded from the NOAA CoastWatch Browser in MATLAB format. NOAA CoastWatch data is available at

http://coastwatch.pfel.noaa.gov/. Each SST pass was analyzed for cloud cover. If a pass had relatively low cloud cover within the CENC domain, it was flagged to be used in the analysis. These good images were used because of the high probablility that independent SST measurements from the satellites will be available for the location we need. If we included every SST image, including the cloudy ones, then few SST measurements would be available for comparison. After SST images were downloaded and good images selected for each case study, the images were masked using the CENC area.

2. HF Radar Data

As mentioned above, the HF radar data used in this thesis originates with the California Ocean Currents Monitoring Program (COCMP). This data is available at *http://www.cencalcurrents.org/*. Data was downloaded as individual radial files for every hour within the case study periods. A single file contained radar data for one hour from a single radar site.

C. CASE STUDIES

To test the hypothesis that current data could be used to improve SST predictions, test cases were needed.

1. CENC Domain

Our area of study is the coastal ocean of central California from Point Sur to Point Arena and out to sea approximately 100 nautical miles. This area, termed the CENC domain, is the approximate limit to the HF Radar's spatial coverage. High resolution satellite SST data (approximate resolution is 1.5 km) is available for this region from the POES AVHRR.

2. Dates of Study

Two time periods were chosen for our study. These case study periods were chosen because of relative abundance of both HF Radar data and clear satellite SST

images. The limiting factor in case study selection is the number of clear SST images available for comparison. The SST data from these case study periods contain a high number of very clear images, necessary for comparison of advected SST pixels with SST measured from satellites. The case study periods were October 17-28, 2006 and January 9-29, 2007.

In the October 2006 case study, there are a total of 43 POES satellite passes with an average cloud cover of 47.5% within the CENC domain. Of these 43 satellite passes, 11 passes were flagged to be used in the study. These 11 images have an average cloud cover of 8.9%. In the January 2007 case study, there are a total of 74 POES satellite passes with an average cloud cover of 57.6% within the CENC domain. Of these 74 satellite passes, 19 passes were flagged to be used in the study. These 19 images have an average cloud cover of 11.9%.

Figure 12 shows a plot of the normalized radar current data coverage for this region for the time periods of the study. The colored squares in Figure 12 represent the percentage of time a radar measurement was available for the different case studies. The white outline is the limits of the CENC region.

3. Stommel Ocean Model

An analytical ocean current field was needed to compare currents generated by the Totals and OMA method to an analytical solution. While any vector field with no-flow boundary conditions could be used, the Stommel ocean model was chosen because of its familiar use in oceanography. The Stommel ocean model was first introduced by Henry Stommel to study the causes of a phenomenon known as westward intensification [9]. Westward intensification refers to the tendency of large-scale ocean circulation to form fast, narrow, and deep currents on the western edge of ocean basins and slow, wide, and shallow currents on the eastern edge of ocean basins. The model assumes a rectangular ocean with wind stress, Coriolis, gravitational, and frictional forces. The component of flow normal to any of the ocean boundaries is necessarily zero. Wind stress forces are defined to be purely in the east-west direction as,

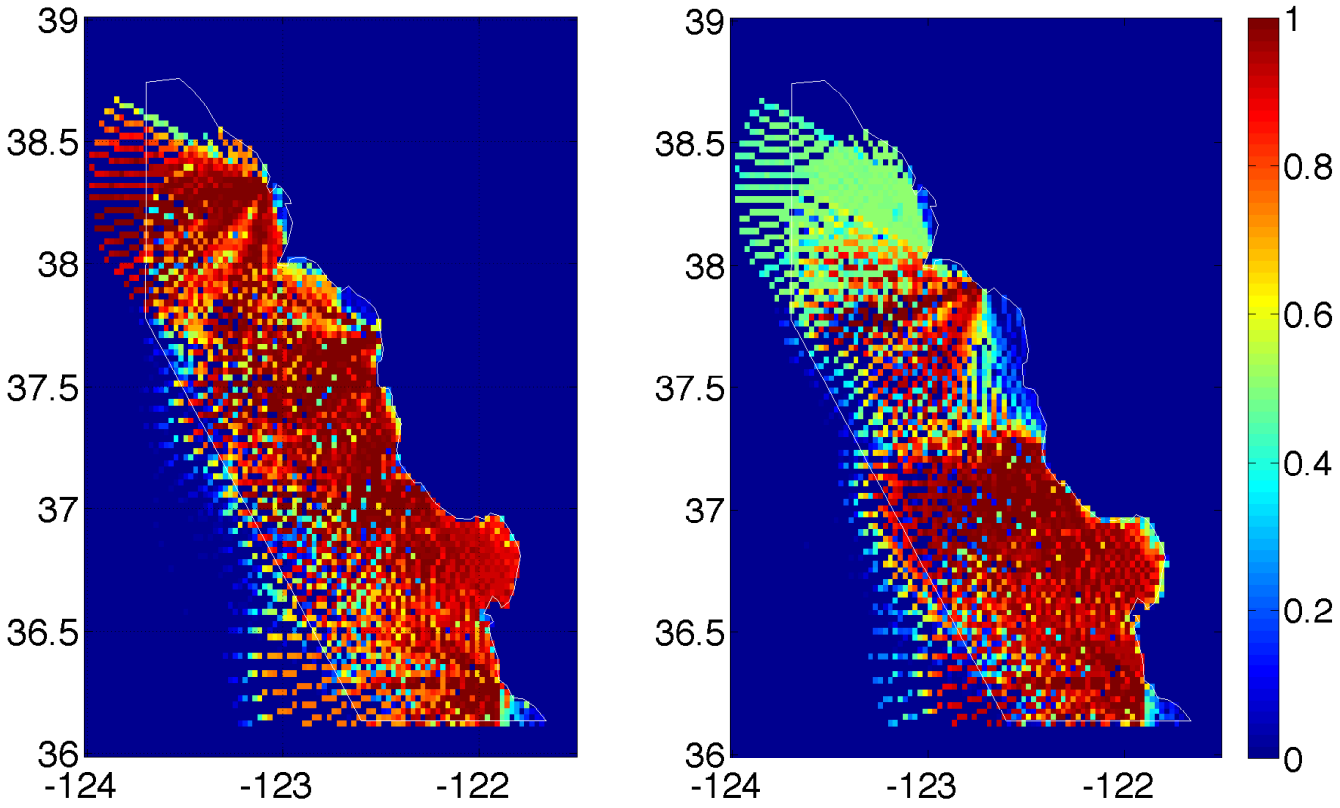

(*a*) (*b*)

Figure 12. Radar data coverage for the central California region. ***a.*** October 17-28, 2006 ***b.*** January 9-29, 2007

$\tau = -\cos\left(\frac{\pi y}{L}\right)$, westward in the bottom part of the ocean, and eastward in the top part of the ocean. With these assumptions, the model can be represented by the equation:

$$\gamma\nabla^2\Psi + \beta\frac{\partial\Psi}{\partial x} = -\frac{\tau_0\pi}{L}\sin\left(\frac{\pi y}{L}\right). \tag{III.2}$$

Ψ is a stream function which describes the current velocity, τ_o is the maximum amplitude of wind stress, γ is the bottom friction coefficient, β is the variation of the Coriolis parameter with latitude, and L is the length and height of the domain. A

steady-state analytic solution to this equation is possible. The u and v components of the steady-state solution are:

$$u = -\frac{\partial \Psi}{\partial y} = \left(-\frac{\pi}{L}\right)\left(c_1 e^{\lambda_1 x} + c_2 e^{\lambda_2 x} + c_3\right)\cos\left(\frac{\pi y}{L}\right) \tag{III.3}$$

$$v = \frac{\partial \Psi}{\partial x} = \left(c_1 \lambda_1 e^{\lambda_1 x} + c_2 \lambda_2 e^{\lambda_2 x}\right)\sin\left(\frac{\pi y}{L}\right) \tag{III.4}$$

where

$$\lambda_{1,2} = -\left(\frac{\beta}{2\gamma}\right) \pm \sqrt{(\frac{\beta}{2\gamma})^2 + (\frac{\pi}{L})^2} \tag{III.5}$$

$$c_1 = -\left(\frac{\tau_o L}{\gamma \pi}\right)\left(\frac{e^{\lambda_1 L} - 1}{e^{\lambda_2 L} - e^{\lambda_1 L}}\right) - \left(\frac{\tau_o L}{\gamma \pi}\right) \tag{III.6}$$

$$c_2 = \left(\frac{\tau_o L}{\gamma \pi}\right)\left(\frac{e^{\lambda_1 L} - 1}{e^{\lambda_2 L} - e^{\lambda_1 L}}\right) \tag{III.7}$$

$$c_3 = \left(\frac{\tau_o L}{\gamma \pi}\right). \tag{III.8}$$

A fictitious rectangular ocean domain was created and used to simulate steady state Stommel-like circulation. To provide a geophysical context, the fictitious ocean was given longitude boundaries of $-124°$ West to $-123°$ West and latitude boundaries of 36° North to 37° North (Figure 13). It should be noted that the Stommel ocean model is used to model oceans on an ocean basin-wide scale. The size of our domain is significantly smaller and the Stommel model does not have a physical context on these scales. The Stommel model was chosen purely for its analytic current field and familiarity to those in the field of oceanography.

The ocean surface flow at any point was calculated using equations III.3 and III.4. Within the ocean model, a subdomain was mapped out for testing of the HFR current generation methods. This subdomain had open boundaries on all sides except the southern boundary, which was shared with the larger ocean domain and is a closed boundary.

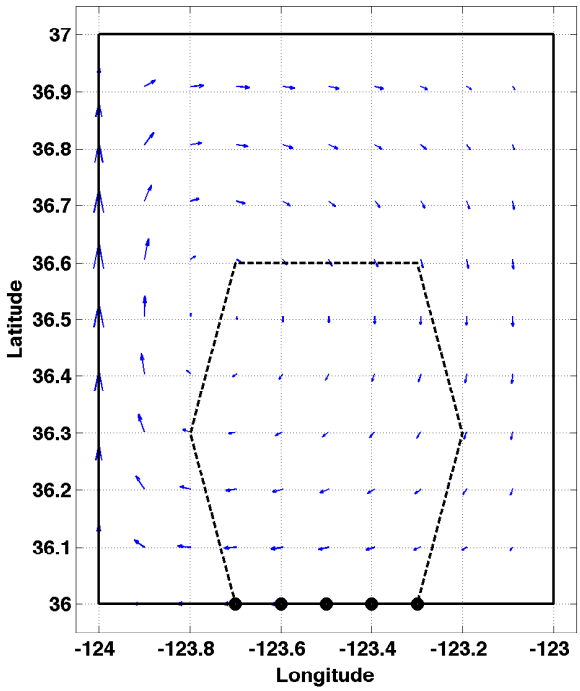

Figure 13. Stommel Ocean model and sample HF Radar domain

On the southern boundary, five radar sites were placed at regular intervals. These sites were used to sample the current velocity field based on typical resolutions of HF Radars. For each radar site, a radial grid of points was created. The radial grid points were spaced at 5° angles between radial 'spokes' and 3 kilometers distance between radial range rings. This spacing is typical of the radar measurement resolution seen on the Central California coast. At these radial grid points, the Stommel field was sampled and the component of the total current velocity in the direction of the bearing line between radar site and grid point was recorded. The component of the velocity along the bearing line is:

$$r = |\boldsymbol{u}| \cos(\phi - \theta), \tag{III.9}$$

where $|\boldsymbol{u}|$ is the magnitude of the current velocity sampled from the Stommel field using equations III.3 and III.4, ϕ is the heading from the radial grid point to the radar site, and θ is the direction of the current vector. A positive radial component points from the radial grid point to the radar site. All angles are measured in the traditional mathematical sense of counterclockwise from East.

After sampling of the Stommel current field, each radar site had measurements of the radial current components at the locations of the radial grid points. A random error was added to each radial measurement to simulate instrument or sampling noise. The random error was uniformly distributed from -10% to +10%. In addition, a certain percentage of random radial measurements were thrown out to represent missing data. The error and missing data were added to attempt to represent physical reality, which contains erroneous and missing data. These radial measurements were then processed back to the current field using either the Totals Method or the OMA Method. A time-series of the Stommel current field was built representing 15 days of data with a sampling every hour, for a total of 360 measurements. While each sampling of the Stommel current field sampled a steady-state field, the current field resulting from the Totals or OMA method was different for each hour's data, due to the random error and missing measurements introduced. The OMA and Totals method were analyzed under these differing conditions to see which method proved more robust to erroneous or missing data.

D. MATLAB PROCESSING

In processing the current data, we used the 'HFR Progs' MATLAB toolbox developed by Dr. David Kaplan. 'HFR Progs' is a toolbox for the processing, viewing, and analysis of HF Radar Currents. The latest version is available at *https://cencalarchive.org/∼cocmpmb/COCMP-wiki*. It provides functionality to process radial current measurements to total currents and particle trajectories using the totals method, as well as functionality to compute OMA modes and fit radial data

to OMA modes and calculate trajectories based on the OMA fits. All processing was completed using either MATLAB 7.0 or MATLAB 7.4.

1. Processing of Radial Data

Radial current data was obtained from the COCMP Web Archive for the two case studies. Each radar data file contains one hour's worth of radial surface current for one radar site. Before the radial files are processed to Total currents or fit to OMA modes, they are cleaned. The radial measurements are cleaned by removing any measurements greater than 100 cm/sec, which is a reasonable upper bound on current velocities for the CENC region [10]. All radial measurements from each radar site are also cleaned using a masking polygon unique to each radar site. The masking polygon for each site represents the area of reasonable data coverage. Occasionally, the radar will report data from areas which are unreasonable, such as current data lying over land. If the radial data file contains measurements that lie outside the masking polygon, these measurements will be removed in this masking step. Finally, radial data was interpolated to fill in gaps. Interpolation was accomplished using the closest values in the bearing direction (filling in a maximum of two missing bearing bins) and in the range direction (filling in a maximum of one missing range bin).

2. Processing to Totals Currents

Cleaned, masked, and interpolated radial current measurements were then processed to total currents using the least-squares fit described in Chapter II, section C. Currents were generated for every hour of each day of the case study time periods. The currents were generated on a regular latitude/longitude grid with two and a half kilometer spacing, which is comparable to the native resolution of the radar observations [3]. In order to make a total current measurement at a grid point, it was specified that at least three radial measurements from at least two different radar sites were required. All radial measurements within three kilometers of a grid point were used in each total current generation. With this search radius, it is possible that a

single radial measurement may have been used in making total current measurements at multiple grid points (i.e., neighboring grid results are not completely independent). After currents were generated on the grid for each hour, the total currents were cleaned and masked. The currents were cleaned by removing any current vector with a speed above 100 cm/sec. Total current vectors were cleaned further by removing any current vector with a GDOP error above 1.5, where GDOP was calculated using the two most orthogonal radial measurements (error flag is 'GDOPMaxOrthog' in the HFR Progs MATLAB Toolbox). A GDOP error less than 1.5 corresponds to an angle separation of between 71° and 109°. Any current measurements remaining after the mask was applied were generated from radial measurements with angle separations in that range.

After cleaning, the total currents were again masked with a polygon outlining the CENC domain to ensure that no outlying current vectors remained. These currents were then interpolated in space and time to fill in any holes in the space/time vector current grid. The interpolation method uses bilinear interpolation in space and time, and then takes the average of the two.

3. OMA Modes Processing

The HFR Progs Toolbox was used to generate OMA modes on the CENC and the Stommel domain. This toolbox makes heavy use of MATLAB's PDE Toolbox to generate the adaptive mesh and to solve the PDE eigenvalue problems of equations II.13 and II.14. MATLAB's PDE Toolbox uses a finite element method to numerically solve eigenvalue PDEs such as this. Certain parameters are required in the modes calculation. The modes were generated with a cutoff scale of five kilometers. A seed value for the estimated number of triangles in the unstructured mesh was given as 10,000 triangles. The method first generated a triangular mesh to use in the mode generation. The MATLAB toolbox uses a Delaunay triangulation algorithm to generate the mesh. Figures 14 and 15 show the triangular mesh generated for the entire domain and for a closeup of the Monterey Bay.

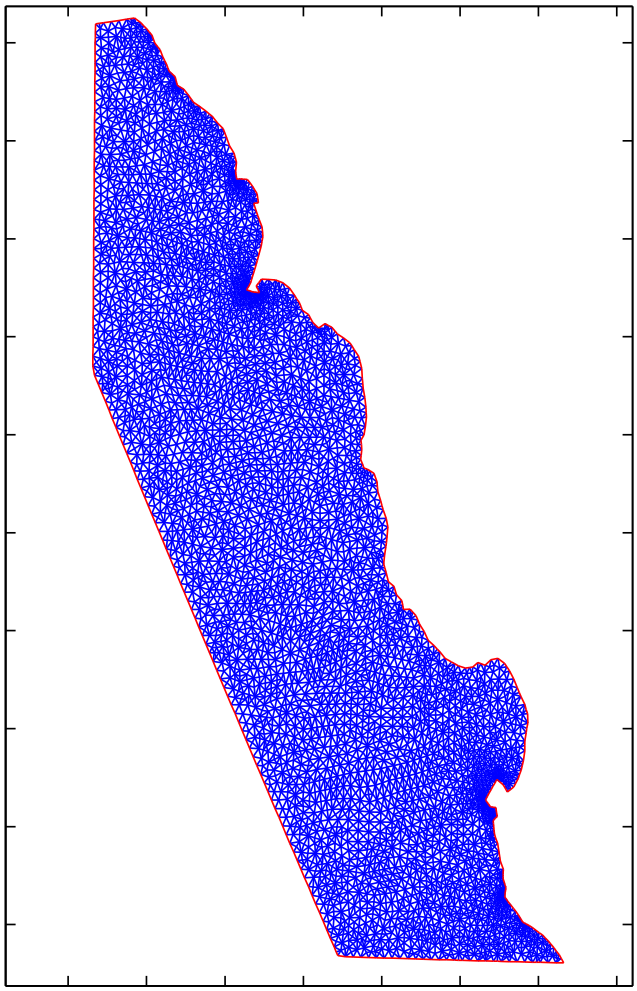

Figure 14. Triangular Mesh for CENC region.

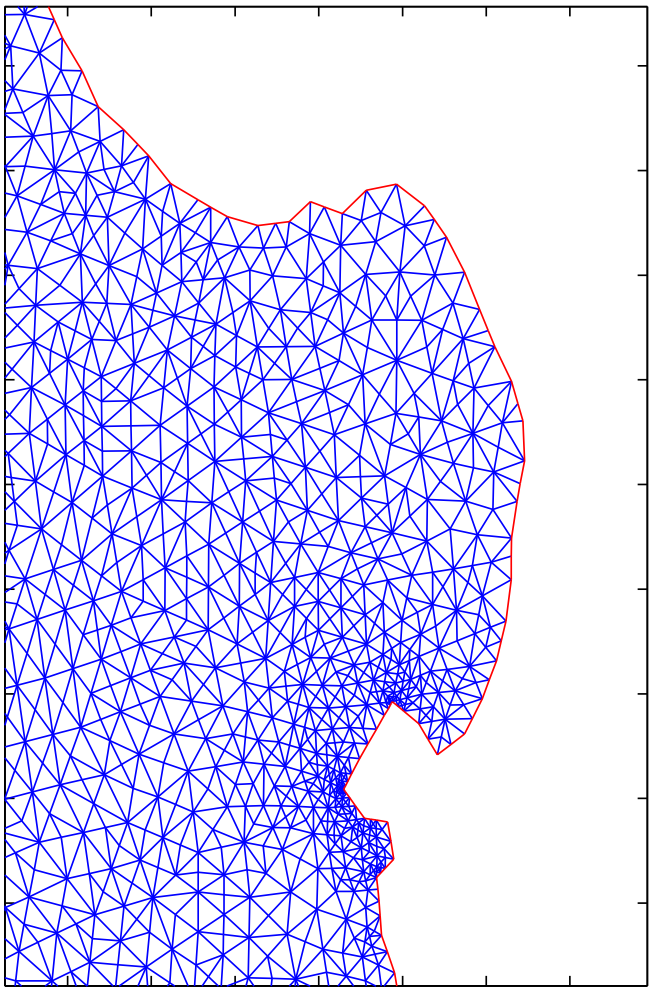

Figure 15. Close-up of Triangular Mesh for the Monterey Bay.

Modes were then generated on this triangular mesh. This resulted in 84 boundary modes, 576 Dirichlet (divergence-free) modes, and 653 Neumann (vorticity-free) modes for a total of 1,313 modes. This is a larger number of modes for a larger area than previously attempted with HF Radar data. The largest scale modes are plotted in Figures 16, 17, and 18.

Modes were also calculated for the hypothetical Stommel model using the same parameters.

4. Fitting Radial Data to OMA Modes

For fitting radial data to OMA modes, the radial files were prepared in the same method as preparing for total current generation, except no radial interpolation was performed. A κ value of 10^{-3} was used for the coefficient penalty. The reasoning for this κ value is discussed in chapter IV, section A.

5. Particle Trajectories

The particle trajectories were calculated in a similar way for both the Totals and OMA methods. Once currents were available, both methods used MATLAB's 'ode45' function to solve the advection differential equation II.30. The MATLAB 'ode45' function is a Runge-Kutta (4,5) ODE solver which uses Runge-Kutta coefficients developed in [11].

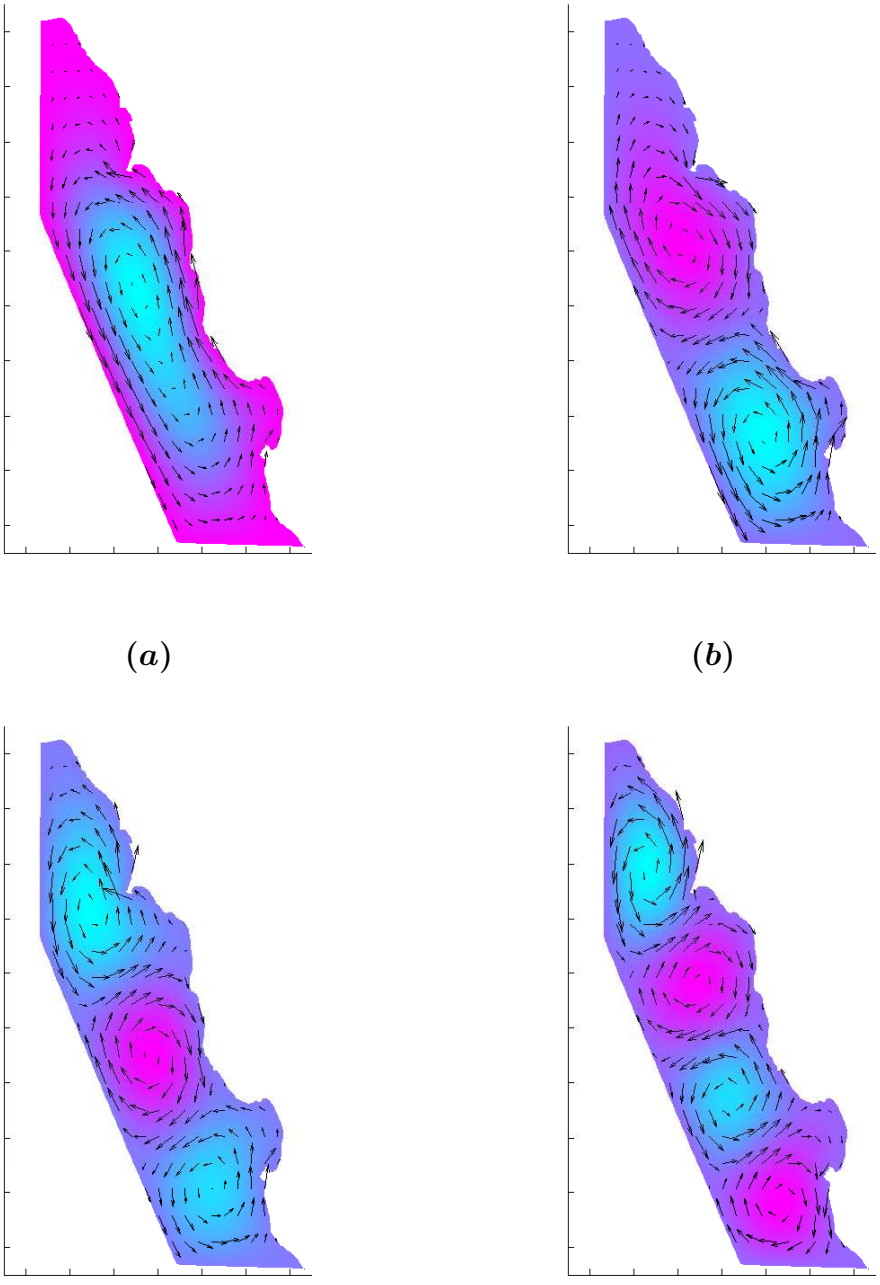

Figure 16. Dirichlet, or Divergence-free modes. ***a, b, c, d*** show the first, second, third, and fourth divergence-free modes: $\psi_1, \psi_2, \psi_3, \psi_4$. Also shown are the corresponding contribution to the current field from these modes in black.

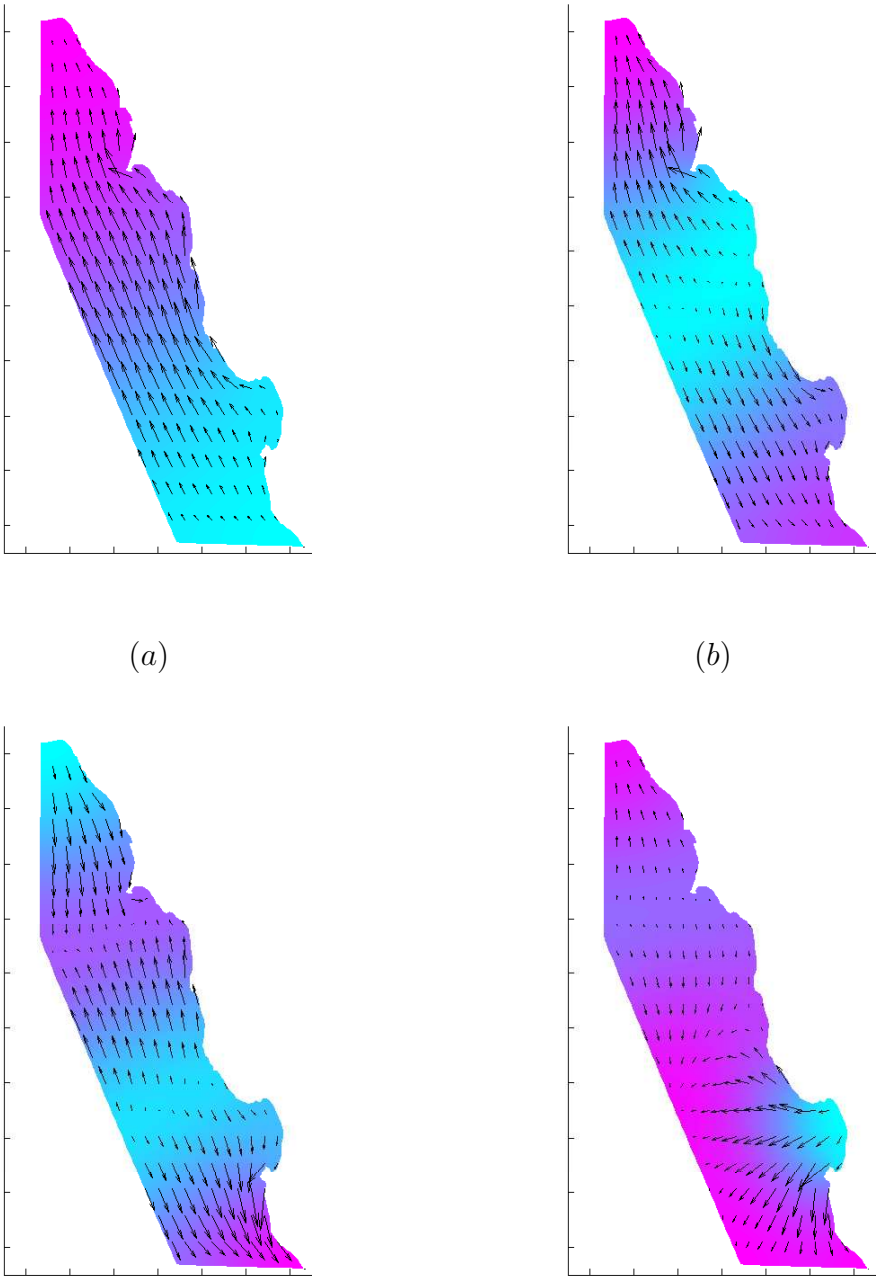

Figure 17. Neumann, or vorticity-free modes. ***a, b, c, d*** show the first, second, third, and fourth vorticity-free modes: $\varphi_1, \varphi_2, \varphi_3, \varphi_4$. Also shown are the corresponding contribution to the current field from these modes in black.

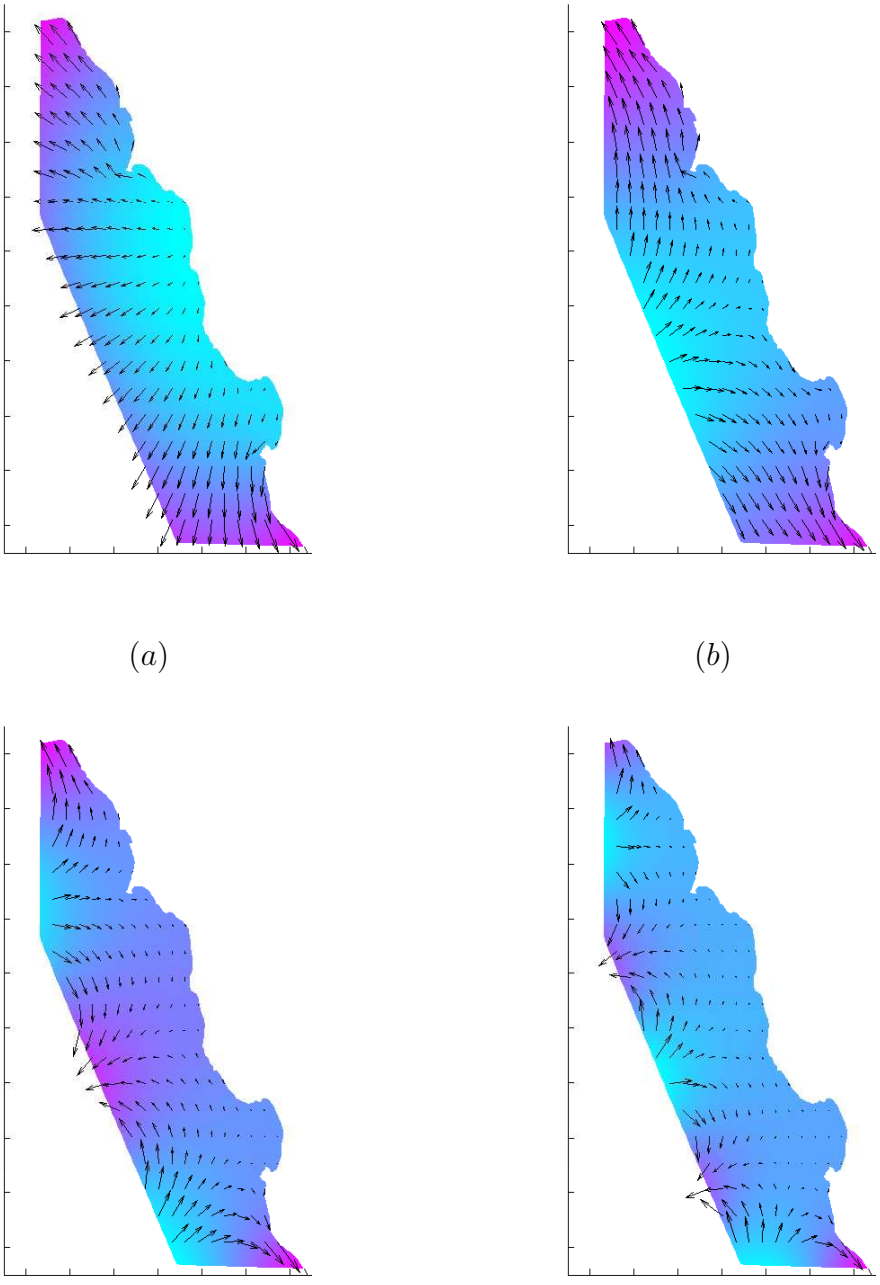

Figure 18. Boundary modes. $\boldsymbol{a, b, c, d}$ show the first, second, third, and fourth boundary modes: $\varphi_1^b, \varphi_2^b, \varphi_3^b, \varphi_4^b$. Also shown are the corresponding contribution to the current field from these modes in black.

IV. RESULTS

A. STOMMEL MODEL CURRENTS

1. Current Statistics

Using an analytic solution and calculating Totals and OMA currents from this solution allowed for direct comparison of the currents and the analytic solution. Radial measurements were sampled from the (steady-state) analytic solution and used to build up currents using the Totals and OMA method. Current magnitudes for the analytic solution in the Stommel subdomain range from 0 cm/sec to 80 cm/sec, with typical values in the 20 - 30 cm/sec range. Error and sampling holes were introduced as described in Chapter III, section 3. The percentage holes varied from 0% to 90% in increments of 10%. The resulting current fields were then compared against the analytic solution. Statistics were calculated for the magnitude of the difference vector of the Total and OMA current field and the analytic solution. These statistics are presented in Tables I and II. The RMS statistic is the RMS of the magnitude of the difference vector, and mean error is calculated as the mean of the ratio of the magnitude of the difference vector and the magnitude of the analytic velocity vector.

% Radial Holes	% Missing Totals Points	Max Difference Vector	RMS Difference	Mean Error
0%	0.0%	1.7 cm/s	0.3 cm/s	5.9%
10%	0.3%	2.2 cm/s	0.3 cm/s	6.3%
20%	0.8%	2.6 cm/s	0.4 cm/s	6.8%
30%	1.7%	3.0 cm/s	0.4 cm/s	7.4%
40%	2.9%	3.4 cm/s	0.5 cm/s	7.8%
50%	6.1%	4.1 cm/s	0.5 cm/s	8.3%
60%	13.3%	4.7 cm/s	0.6 cm/s	8.1%
70%	23.2%	4.6 cm/s	0.6 cm/s	7.3%
80%	44.6%	4.4 cm/s	0.6 cm/s	5.0%
90%	78.3%	6.7 cm/s	1.0 cm/s	1.9%

Table I. Statistics for Totals Currents calculated on Stommel domain.

% Radial Holes	% Missing Totals Points	Max Difference Vector	RMS Difference	Mean Error
0%	0%	41.3 cm/s	0.8 cm/s	11.6%
10%	0%	41.0 cm/s	0.8 cm/s	11.9%
20%	0%	40.3 cm/s	0.8 cm/s	12.3%
30%	0%	40.0 cm/s	0.9 cm/s	13.0%
40%	0%	39.5 cm/s	0.9 cm/s	13.8%
50%	0%	39.7 cm/s	1.0 cm/s	14.9%
60%	0%	41.4 cm/s	1.1 cm/s	17.0%
70%	0%	47.0 cm/s	1.2 cm/s	19.4%
80%	0%	60.4 cm/s	1.5 cm/s	25.5%
90%	0%	134.0 cm/s	2.6 cm/s	44.9%

Table II. Statistics for OMA Currents calculated on Stommel domain.

2. Totals Currents Reconstruction

Tables I and II reinforce that the Totals method is a local fit method, while the OMA method is a global fit method. It is seen from Table I that the Totals currents are a good approximation for the analytic currents even when a large percentage of the radar measurements that go into making Totals currents are removed. This is reflected in the low RMS difference and mean error entries. An interesting feature of the Totals method is reflected in the mean error column. As the number of holes increases, the mean error of the measurements also increases, but then starts to decrease as the percentage of radial holes grows past 50%. Due to the spacing and location of the radar sites, the final current measurements become concentrated in the lower half of the domain. Even when 90% of radial measurements are removed, more than enough radial measurements exist to generate currents in the southern portion of the domain. This leads to a very good fit in the lower part of the domain, and no measurements at all in the rest of the domain, hence the lower mean error. The biggest drawback to this method is the large amounts of missing data that result when sparse radial coverage is available. Figure 19 shows two reconstructed current fields using the Totals method on the Stommel field with 0% and 90% holes. These are single time slices of the fields which give rise to the statistics in Table I, rows one

and ten. The reader is also referred back to Figure 13 in Chapter III, section C for a plot of the analytic Stommel currents.

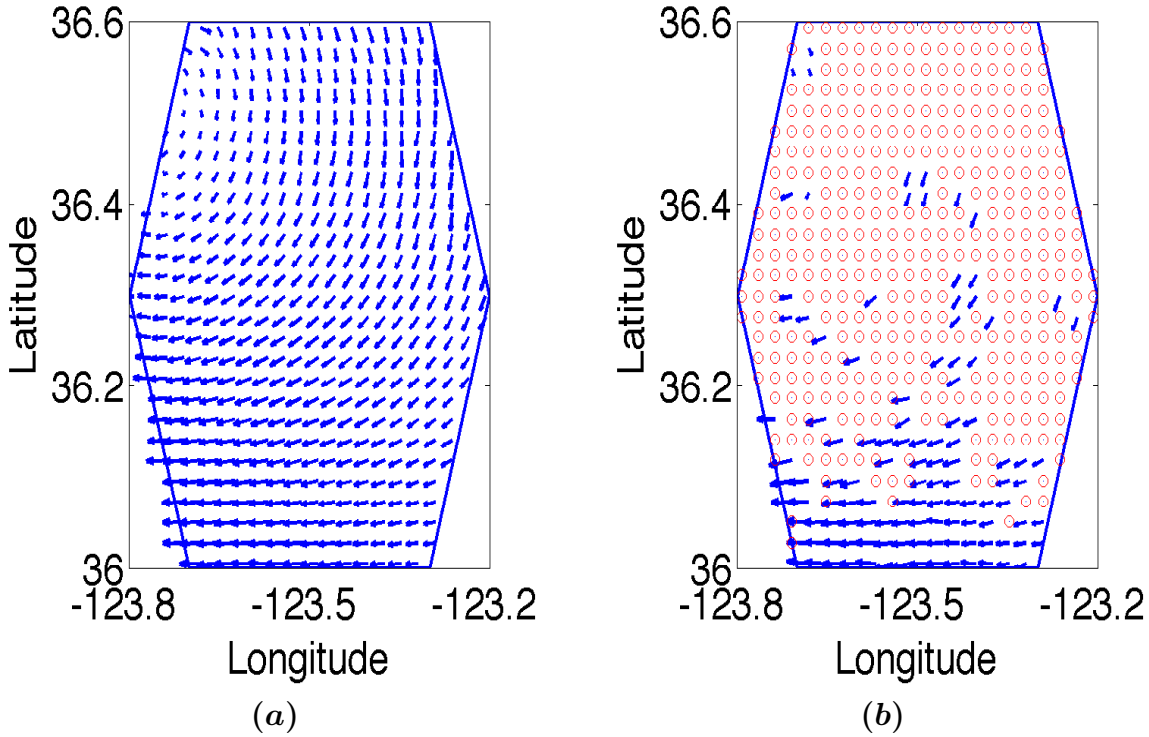

Figure 19. Reconstruction of Stommel current field using Totals method. **(*a*)** Current field sampled with 10% error and 0%holes. **(*b*)** Current field sampled with 10% error and 90% holes.

3. OMA Currents Reconstruction

In contrast to the Totals method, the OMA method is a global method. All available radial measurements are used in the cost function to find the mode coefficients, α_i, that best fit the modes to available measurements. Because the modes are defined over the entire domain, reducing the number of radial measurements will not reduce the coverage of the OMA currents. As can be seen in the OMA statistics table, however, reducing the number of radial measurements does reduce the accuracy of the OMA fit. These large differences are present in areas with few radial measurements. Even for relatively dense and uniform radial coverage, the OMA method can lead to

large differences for a few current vectors, particularly along the edge of the domain. Figure 20 shows a reconstructed OMA current field for the same Stommel field with 0% and 90% holes. These are the single time slices of the fields which give rise to the statistics in Table II, rows one and ten. It is seen that the domain boundaries, particularly the southwest corner, are hard for the OMA method to fit.

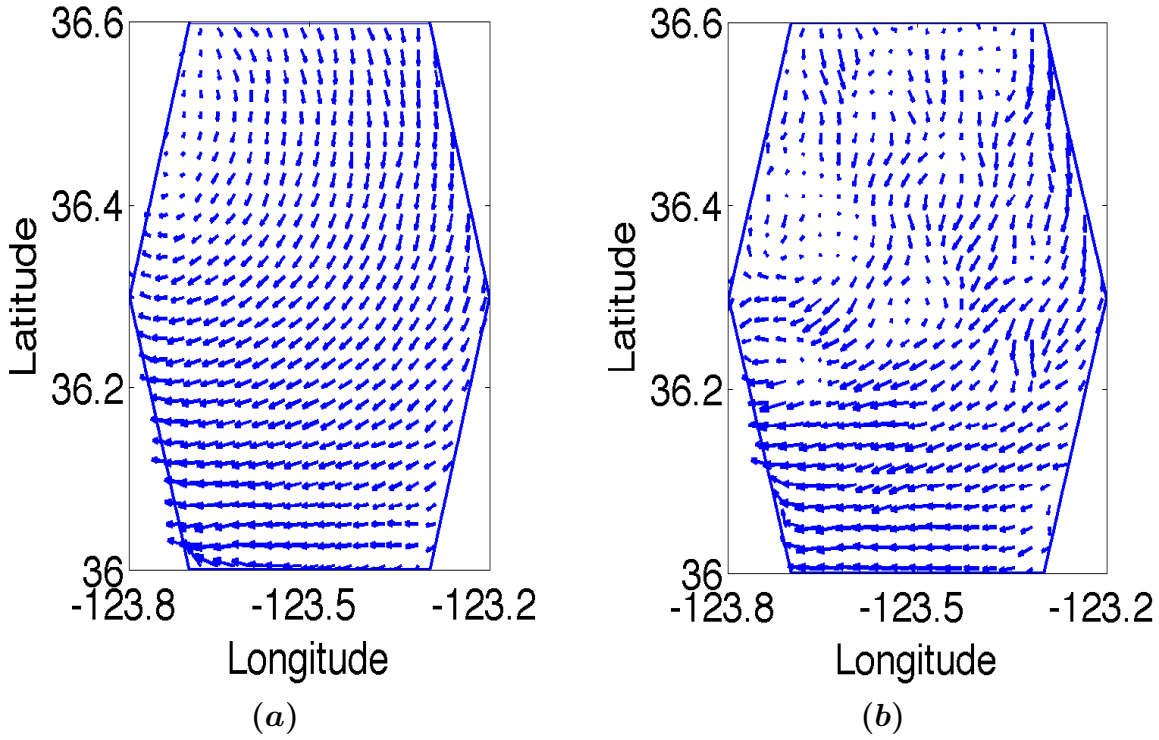

Figure 20. Reconstruction of Stommel current field using OMA method. **(*a*)** Current field sampled with 10% error and 0%holes. **(*b*)** Current field sampled with 10% error and 90% holes.

Figure 21 shows the contribution to the OMA currents from each of the different type of modes: Neumann (φ), Dirichlet (ψ), and Boundary (ϕ^b). The full current field is a sum of these three parts. The modes are fit to the field with 0% radal holes and 10% error (the first row in Table II). From these figures, it is seen that the boundary modes are contributing most to the errors seen in the lower left and lower right portions of the Stommel domain. The Dirichlet and Neumman modes do not have much difficulty in these corners because the boundary conditions that are

imposed on these modes mean that there is no difference between open and closed boundary segments. The Boundary modes, however, do "see" a difference in open and closed boundaries. These corners, where a closed boundary meet an open boundary can be difficult to fit for boundary modes. The biggest errors in the OMA fits occur in these corners, where the boundary modes have difficulty adjusting for the change from closed to open boundaries.

4. Mode Coefficient Penalty

A study was done on the κ parameter for the Stommel domain. Small κ values translate into small penalties for large mode coefficients. If there are few holes and abundant radial coverage, then the measurements naturally limit the mode coefficients from becoming large and the κ term in the cost function is unnecessary. If there are large holes in the radial data coverage, then the κ term is necessary in the cost function to keep mode coefficients and currents from becoming large in areas of little data coverage. However, including a κ term which is too large might suppress mode coefficients below their accurate value. Of course, the extent of data coverage is not known before the time of measurement, so a value for κ should be chosen that both suppresses unrealistically large mode coefficients while allowing those mode coefficients to accurately describe available measurements. Figure 22 shows the RMS difference between OMA currents and analytic currents plotted against the logarithm of κ for varying amounts of missing data. A κ value of $10^{-3} - 10^{-2}$ minimizes the RMS difference of fitted currents with actual analytic currents for a wide range of missing data. A value of 10^{-3} was chosen for this investigation. These results agree with [7], where an analysis of the κ parameter was conducted by comparing OMA and Totals currents for cases near Bodega Bay.

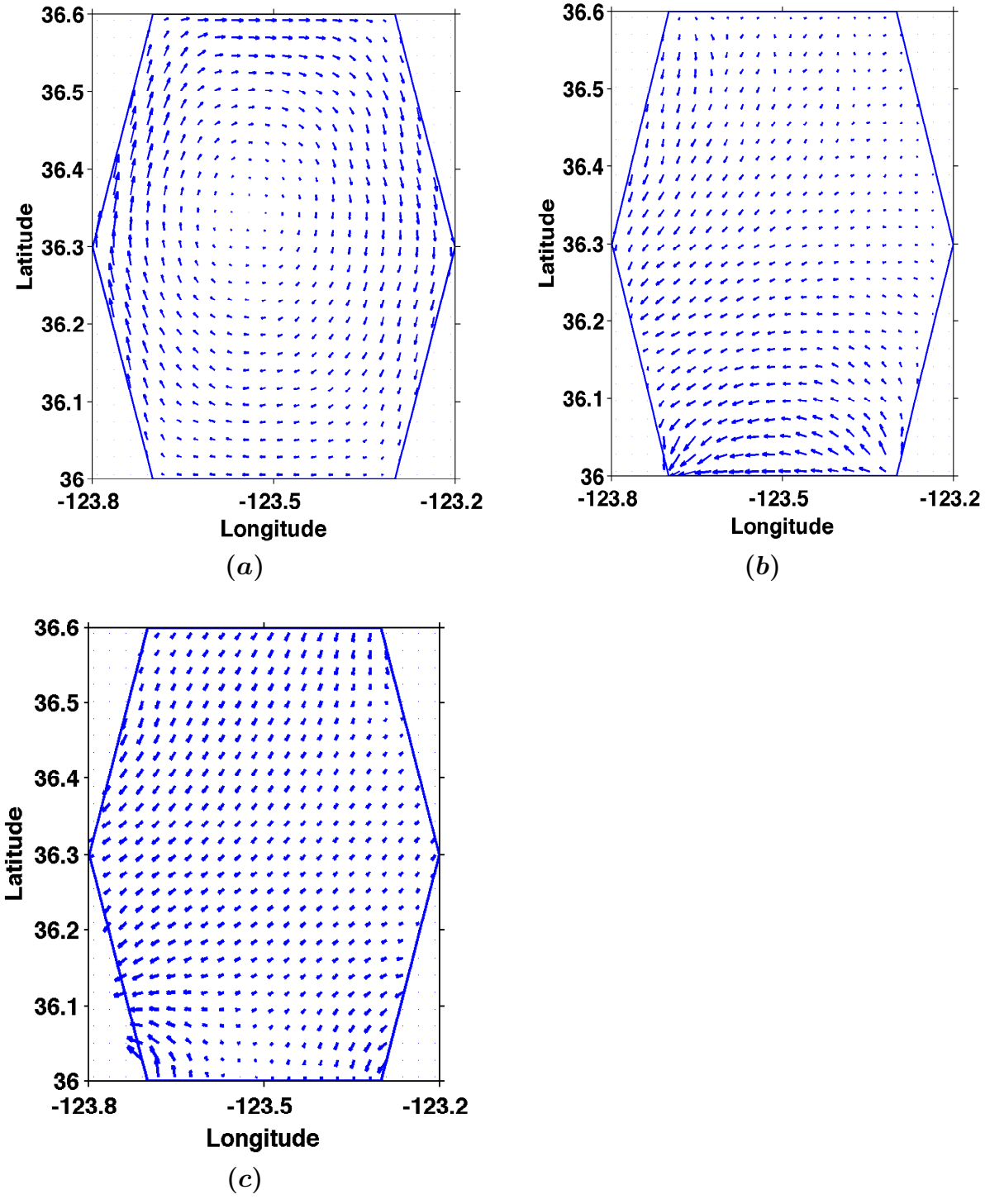

Figure 21. Contributions to the Stommel currents from the different types of modes. ***a.*** Dirichlet (curl or vorticity) modal currents. ***b.*** Neumann (divergence) modal currents. ***c.*** Boundary modal currents.

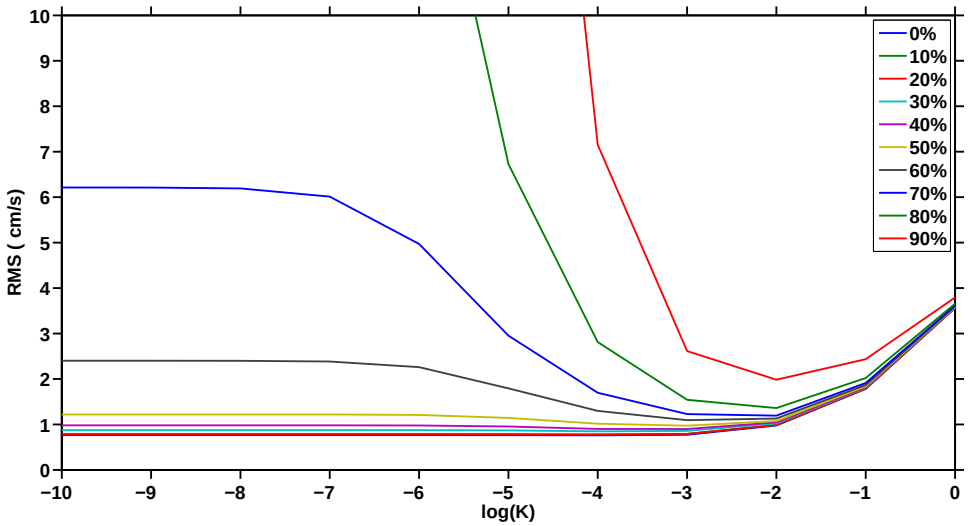

Figure 22. RMS difference of OMA currents and the analytic Stommel solution for varying amounts of missing data.

B. SST COMPARISONS AND MODEL TESTING

Currents and trajectories were calculated for the CENC domain for the October and January case studies. SST comparisons were carried out between all high-quality satellite image pairs in the case studies (both for absolute temperature and temperature anomaly) as described in Chapter III, section A. For the October case study, this resulted in a total of 55 image pair comparisons. For the January case study, this resulted in 171 image pair comparisons. The result of these comparisons were a set of statistics on each pair of SST images that were compared. Figures 23 to 30 show the RMS of the difference of SST points for the difference comparison schemes against the difference in time between compared SST images.

Figures 23 through 26 show the absolute SST comparisons using both Totals and OMA currents for the two different case studies. Figures 27 through 30 show the SST anomaly comparisons using both Totals and OMA currents for the two different case studies.

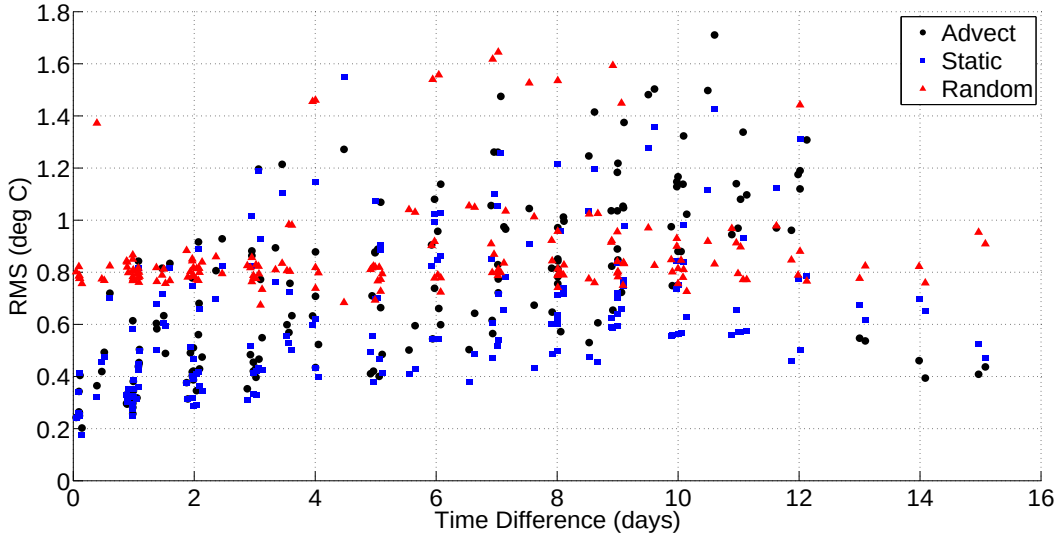

Figure 23. RMS of the difference of SST points using advected, static, and random comparisons. Absolute SST is compared, and particle trajectories are calculated using Totals currents for the January, 2007 case study.

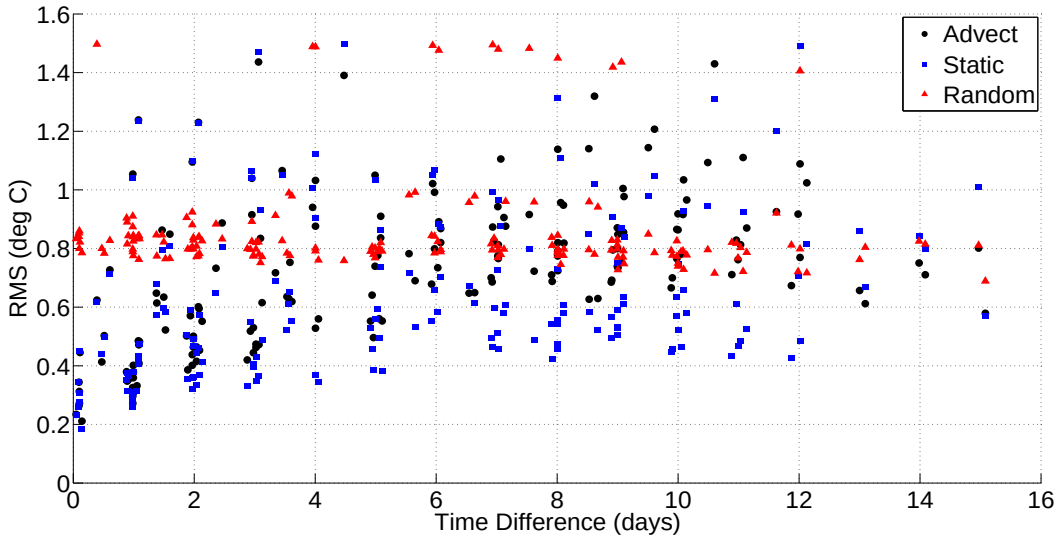

Figure 24. RMS of the difference of SST points using advected, static, and random comparisons. Absolute SST is compared, and particle trajectories are calculated using OMA currents for the January, 2007 case study.

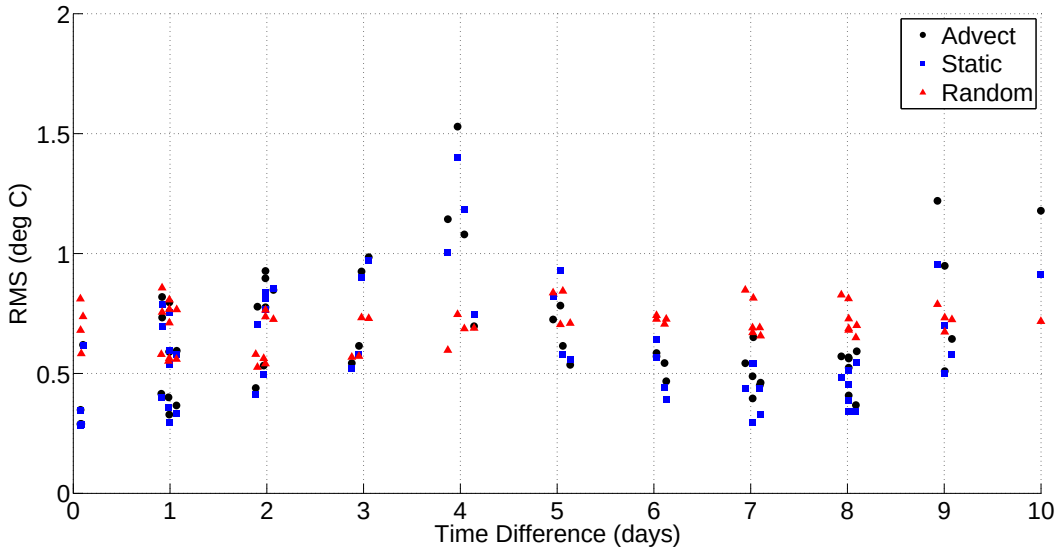

Figure 25. RMS of the difference of SST points using advected, static, and random comparisons. Absolute SST is compared, and particle trajectories are calculated using Totals currents for the October, 2006 case study.

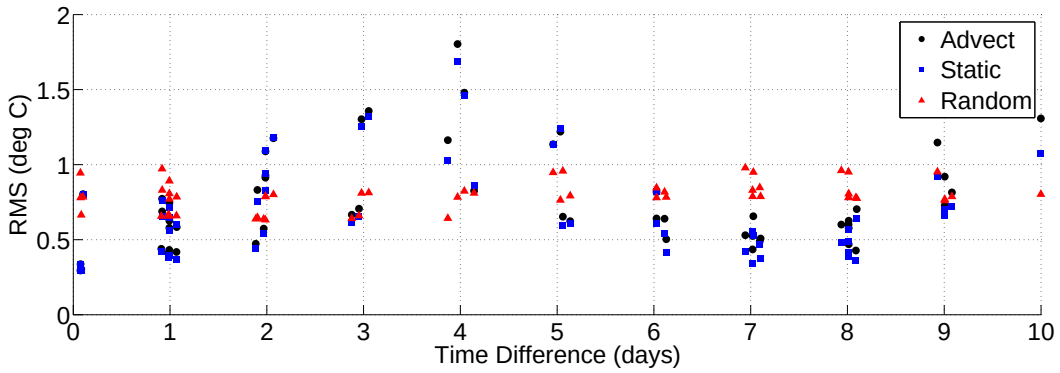

Figure 26. RMS of the difference of SST points using advected, static, and random comparisons. Absolute SST is compared, and particle trajectories are calculated using OMA currents for the October, 2006 case study.

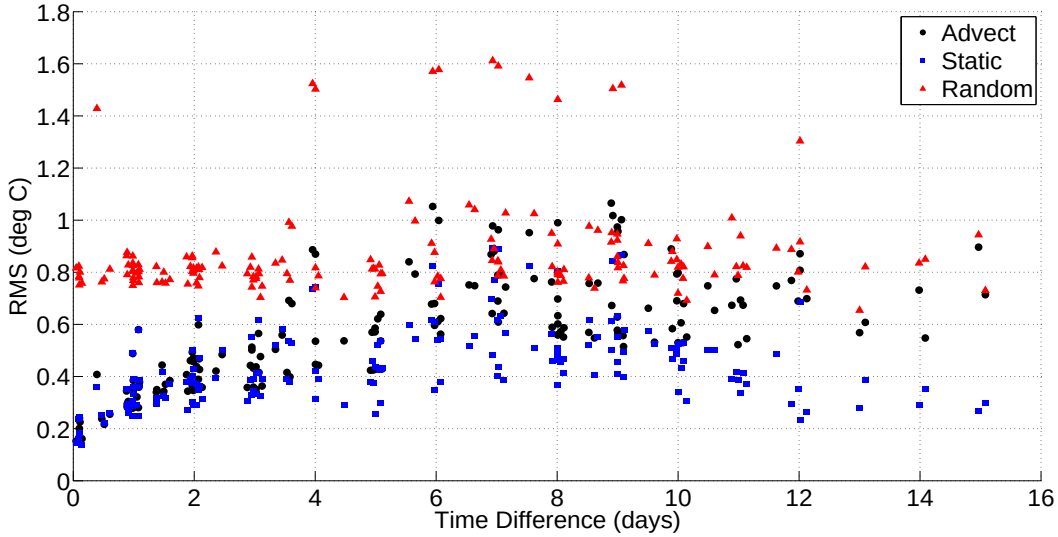

Figure 27. RMS of the difference of SST points using advected, static, and random comparisons. SST anomaly is compared, and particle trajectories are calculated using Totals currents for the January, 2007 case study.

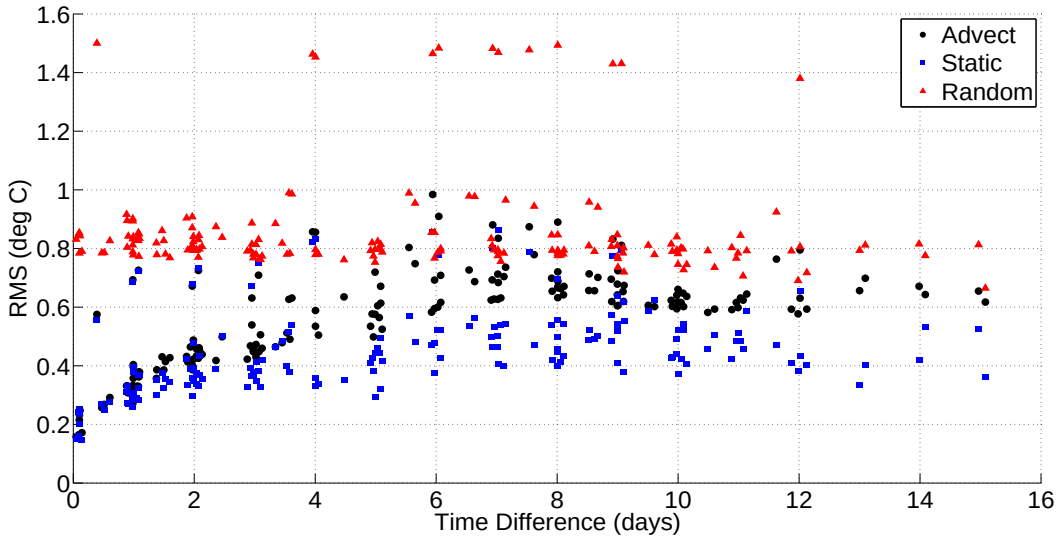

Figure 28. RMS of the difference of SST points using advected, static, and random comparisons. SST anomaly is compared, and particle trajectories are calculated using OMA currents for the January, 2007 case study.

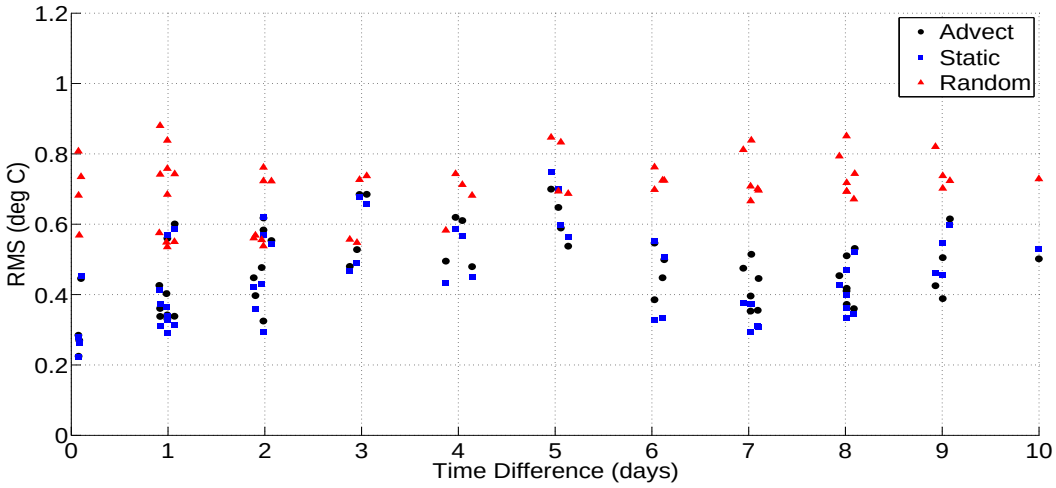

Figure 29. RMS of the difference of SST points using advected, static, and random comparisons. SST anomaly is compared, and particle trajectories are calculated using Totals currents for the October, 2006 case study.

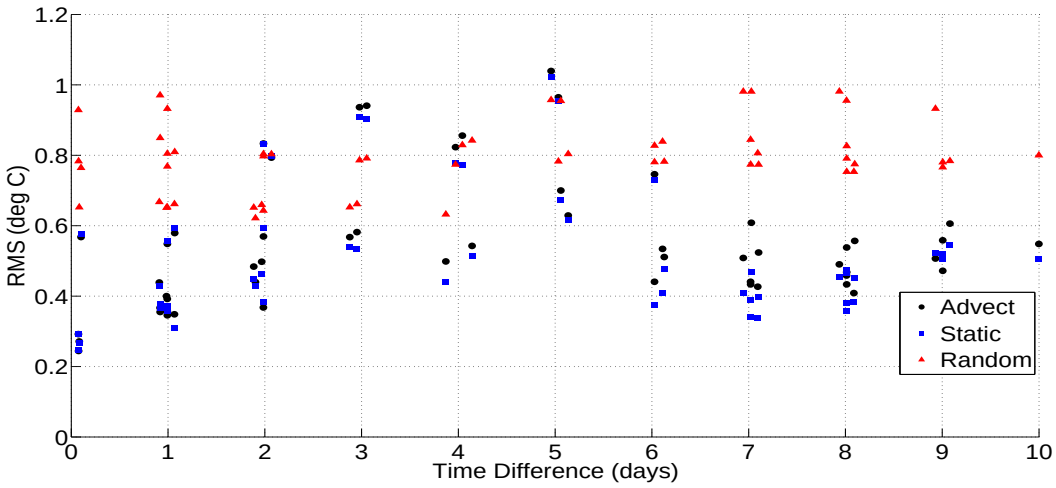

Figure 30. RMS of the difference of SST points using advected, static, and random comparisons. SST anomaly is compared, and particle trajectories are calculated using OMA currents for the October, 2006 case study.

Interpretation of these statistics is difficult, and definite conclusions on a 'best method' impossible. In these SST comparisons, the random comparison is used as a 'baseline' comparison. In the random comparison, SST (or SST anomaly) at the arrival points of the trajectories are compared against another random SST pixel within the image. This serves as a measure of the inherent variability within the image. In the absolute comparisons in the January case study (Figures 23 and 24), the static and advected methods show a general upward trend as the time separation between SST images increases for both OMA and Totals trajectories. There does not appear to be a clear distinction between the advected and static methods for the absolute temperature comparison in January until the time difference reaches approximately 8-10 days, at which point it appears that the static method more regularly leads to smaller RMS values than the advected method, although the points are still grouped together. Static and advected RMS values remain lower than random comparisons until the time difference is approximately 6-8 days, at which point all comparison methods become intermingled.

For absolute temperature comparisons in October, advected and static methods show similar results, starting lower than the random comparisons, rising up higher than the random points around time differences of 3-5 days, then falling again and starting to rise. The reason for the peak at 3-5 days is unclear. In general, it appears that the static method gives lower RMS values than the advected method, although the points are usually grouped close together.

In the SST anomaly comparisons, the approximations of the advected and static methods become more accurate. Anomalies were compared as an attempt to remove the effects of large scale warming or cooling of the SST in our domain. If the entire area was warmed or cooled at a similar rate over the time difference between starting and ending images, then it was hoped that taking the anomaly would account for most of this change. In the January time period, both advected and static methods appear to perform (predict SST) better than a random sampling. For time differences

up to 3-4 days, the two methods are indistinguishable for both OMA and Totals trajectories. After 3-4 days, the static method generates lower RMS differences than the advected method. Both methods seem to do better than the random comparison method. The static method seems to outperform the advected method for all values of time separation, although they are grouped fairly close together. In the October time period, the static and advected methods show a similar pattern as in the absolute comparisons (rising RMS values reaching a peak around 4-5 days, then falling and rising again). In this case, the static and advected methods stay below the random comparison. There is no discernable difference between static and advected methods in this time period.

1. Comparison of OMA and Totals Advected Methods

If the advected method offered improvements over the other comparison methods, then it is expected that the present SST field could be predicted by a past SST field when advection of surface water is taken into account. This, of course, will only work when accurate surface current and particle trajectories are available. As a measure of performance of the two different surface current measurements, OMA and Totals Currents, the advected SST comparisons using both OMA and Totals trajectories are plotted together for the two case studies in Figures 31 to 34. These figures are the same statistics for the advected method presented in Figures 23 to 30. They are extracted and presented on the same figures to ease comparison. Both OMA and Totals currents give rise to similar performance of the advected method for all case studies.

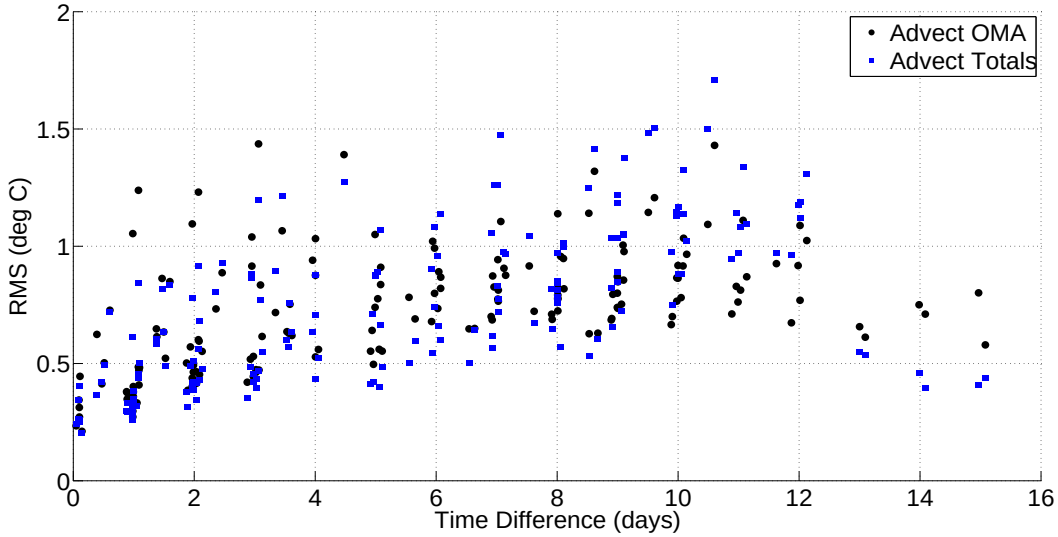

Figure 31. RMS of the difference of SST points using advected comparisons for both OMA and Totals trajectories. Absolute SST is compared for the January, 2007 case study.

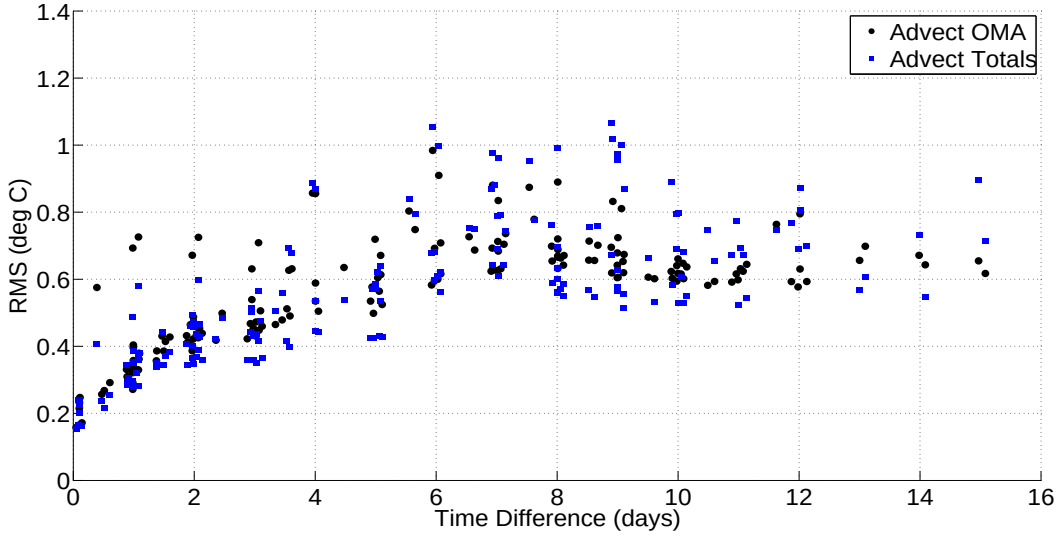

Figure 32. RMS of the difference of SST points using advected comparisons for both OMA and Totals trajectories. SST anomaly is compared for the January, 2007 case study.

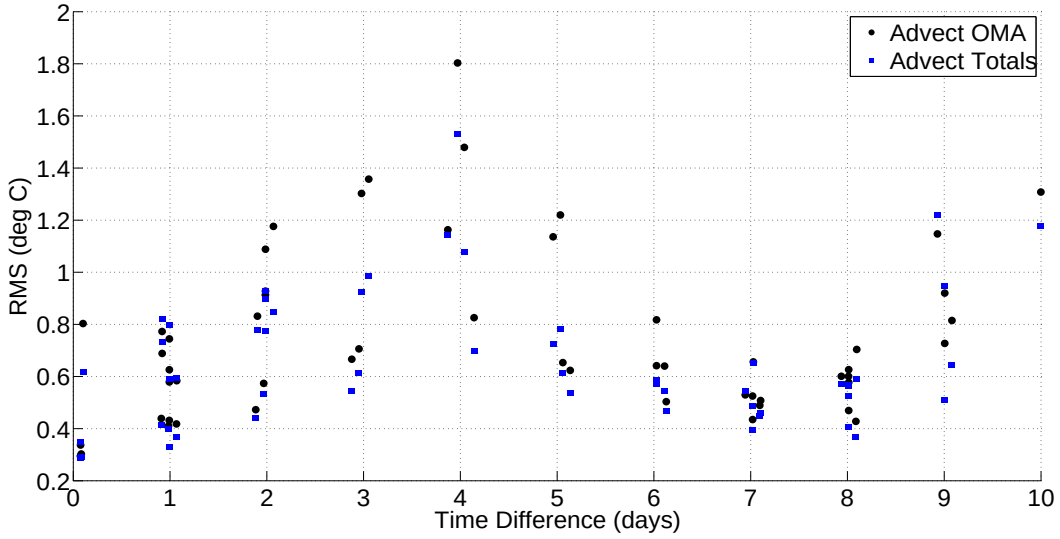

Figure 33. RMS of the difference of SST points using advected comparisons for both OMA and Totals trajectories. Absolute SST is compared for the October, 2006 case study.

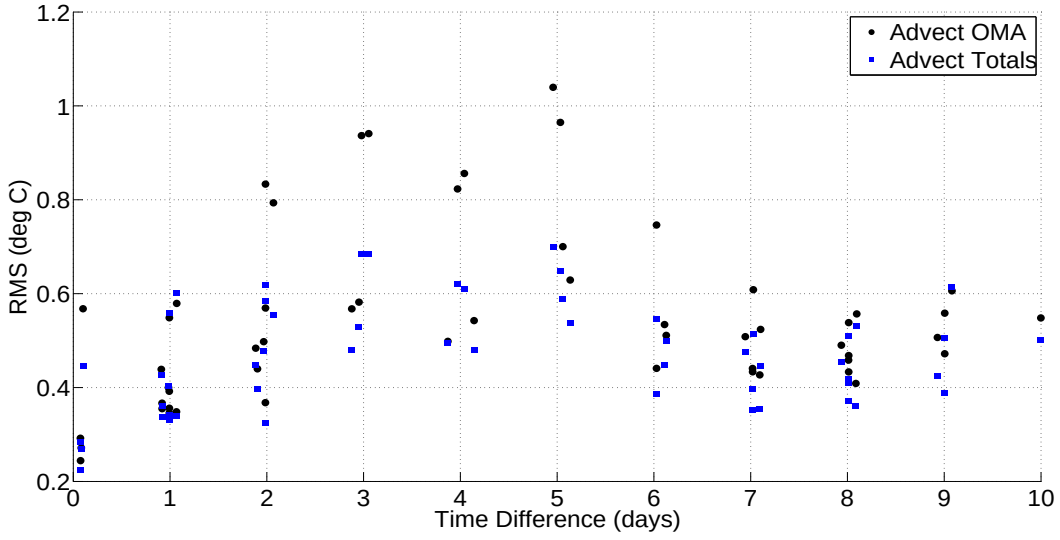

Figure 34. RMS of the difference of SST points using advected comparisons for both OMA and Totals trajectories. SST anomaly is compared for the October, 2006 case study.

2. Calculations on the Distance of Advected Particles

In the advected comparison method, calculations were also completed on the distance individual particles were advected. Individual particle displacement distances were combined into a RMS of advected displacement statistic. These statistics are plotted in Figure 35. Predictably, as time increases, particles are advected further from their starting position, on average.

C. RECONSTRUCTION OF SST FIELD

If the advected model is a good prediction of future SST, then some method is needed to reconstruct the full SST field from the (relatively) few points that are advected from one image to another. Numerous interpolations methods exist for scattered data interpolation. Figure 36 shows the reconstructed and actual temperature field for October 25, 2006, 21:36 GMT. The reconstructed field is generated using the SST points advected (with Totals currents) from October 17, 2006, 21:18 GMT to October 25, 2006, 21:36 GMT. The reconstruction is accomplished using MATLAB's 'griddata' function, which utilizes triangle based linear interpolation.

The reconstructed field and the actual SST field are significantly different. Major features of the actual field (Figure 36d), such as the cold-water plume off Pescadero and Half Moon Bay in the center of the image are absent in the reconstructed image. The reconstructed image might be showing some promise in that locations of SST features such as fronts (areas of high gradient) appear to be in the correct locations, but overall the reconstruction is of low quality. A better approximation would be Figure 36c, which is just the past SST field with no advection information.

An alternative method of reconstructing the SST field is to identify points where the SST is needed, and the find the *backwards trajectory* from that point to a point in a previous image where SST is available. This can be done using the same current information necessary to compute forward trajectories.

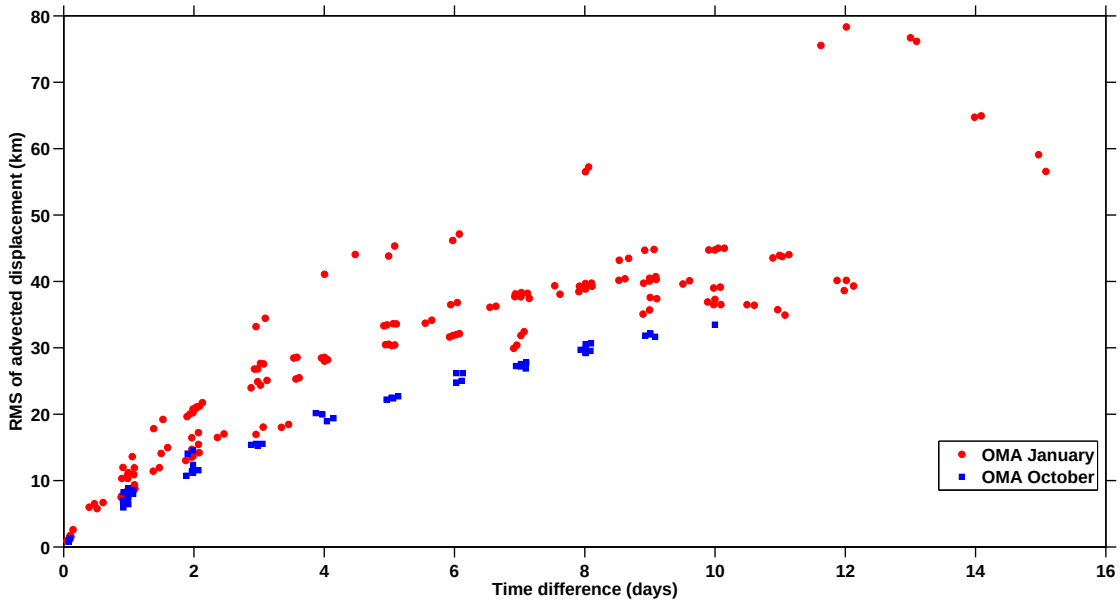

(*a*)

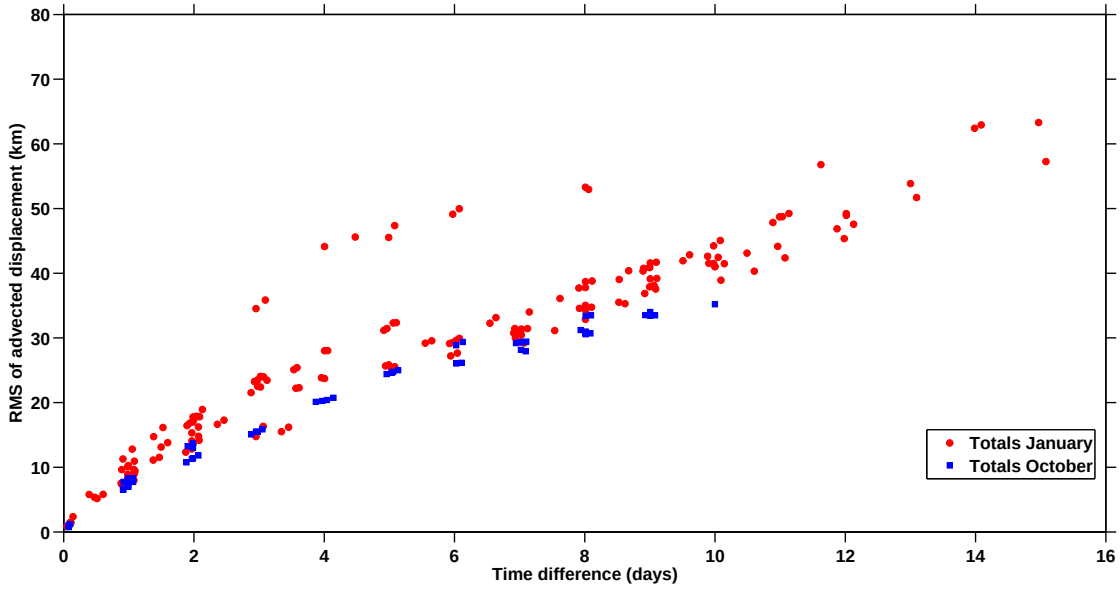

(*b*)

Figure 35. Displacement of advected particles. Particles from both case study periods are shown in each plot. (***a***) Displacement of particles using OMA currents. (***b***) Displacement of particles using Totals currents.

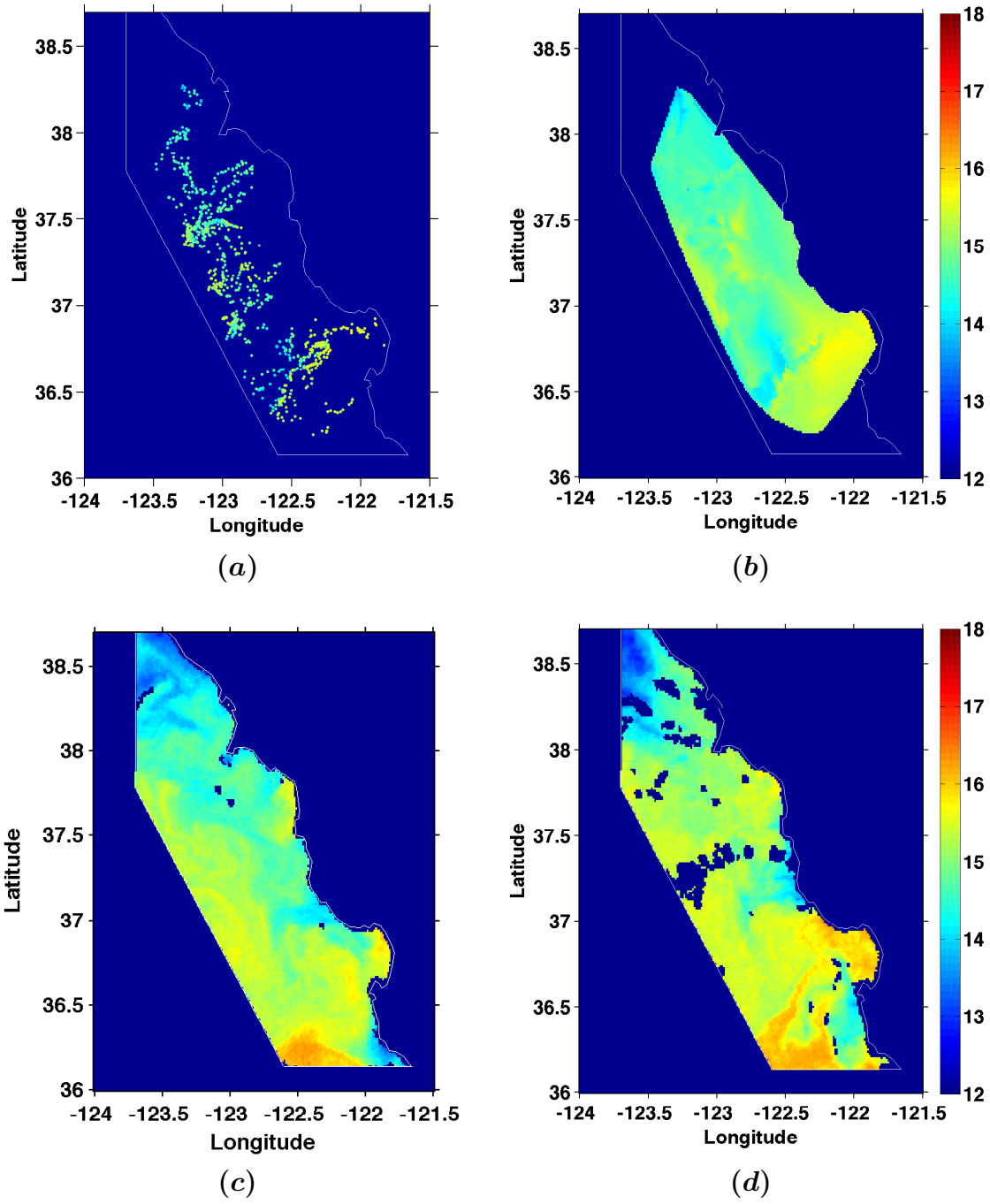

Figure 36. **(a)** Predicted SST field for 21:36 GMT, October 25, 2006, based on particles advected from 21:18 GMT, October 17, 2006. **(b)** Reconstructed temperature field based on advected points in panel (a). **(c)** Actual SST field for 21:18 GMT, October 17, 2006 as measured by satellite. **(d)** Actual SST field for 21:36 GMT, October 25, 2006, as measured by NOAA satellite.

D. RECOMMENDATIONS FOR FURTHER STUDY

1. Refinement of Advection Model

It is seen that the advection SST model proposed is not an adequate predictor of the present or future SST field. It appears that the static model, where the SST at a point is simply modeled by a SST measurement at that same point in the past, does just as well at predicting a future SST value. The static model does not utilize any information about the surface current field. The advected model, in contrast, contains no information on the past SST at that location. Perhaps a model which includes information on *both* the advected SST and static SST would perform well. This is a regression model question. What is the ideal (if any) combination of advected and static SST to be used in predicting future SST?

2. Frontal Advection

Another proposed advection model concentrates the predictions in areas of interest. It is often the case that researchers are more interested in certain features of the SST field than others. These features are typically areas of high temperature gradients, called fronts. Instead of predicting a SST field based on the advected locations of a grid of points spread over the entire domain, the field could be predicted by the advected locations of a set of points that define the feature of interest. The advected locations of the features can be used as control points and the entire image registered based on these control points.

3. Lagrangian Coherent Structures

The method of calculating particle trajectories by integrating the surface velocity can lead to significant errors in the trajectories for small changes in the velocity field, such as those added by measurement error. Studies are underway which seek to calculate the locations of more robust structures in the surface velocity field which are less sensitive to errors in individual current measurements. Some of these structures, called Lagrangian Coherent Structures (LCS), form natural barriers to fluid transport and act as separators of areas of different dynamics. These LCS can be calculated

from the Finite-Time Lyapunov Exponent (FTLE), discussed in [12]. Figure 37 is an example of FTLE and LCS caculations from HF radar current data in the Monterey Bay. Note the LCS running north-south across the mouth of Monterey Bay divides the flow within the bay from the flow which remains outside the bay. LCS can be utilized in SST prediction by helping to guide calculated trajectories, reducing the impact of measurement errors on the overall particle trajectories.

4. Adaptive Interpolation Functions for Scattered Data Interpolation

A different proposed model is related to scattered data interpolation. Instead of modeling a present (but incomplete) SST field by a past field, the present incomplete field might be filled in by interpolation of the measurements that exist in the

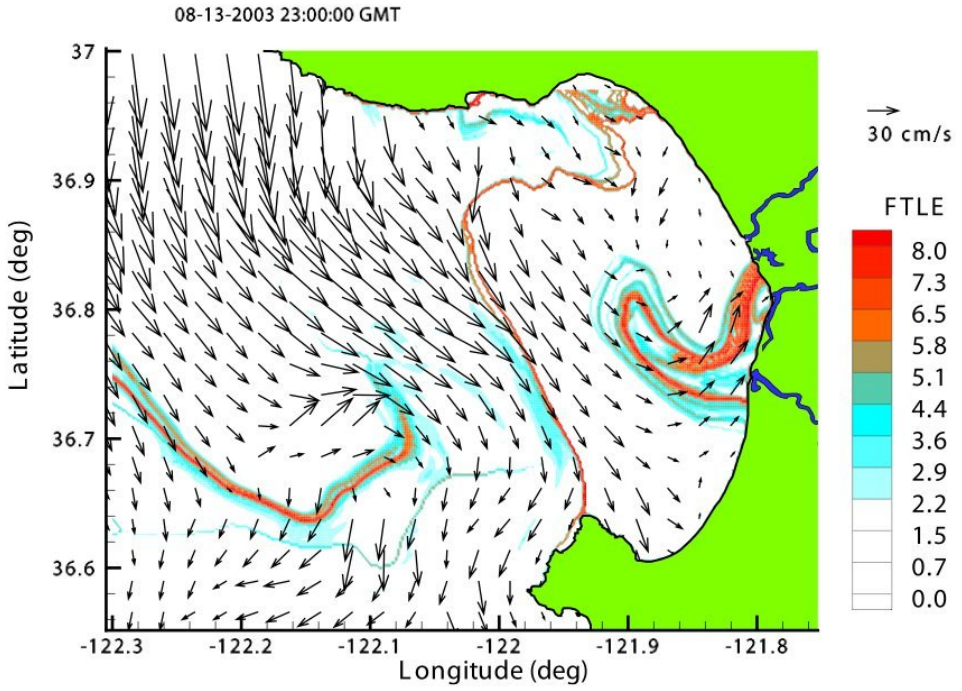

Figure 37. FTLE field computed from HF radar velocity data. Curves of high FTLE represent time-varying LCS. Also shown is HF radar velocity field at the given time. From [12].

present field. Existing interpolation methods might interpolate a value based on a weighting function applied to surrounding measurements. One weighting function is the Gaussian weighting function, which weighs surrounding measurements equally based on the negative exponential of the squared the distance to the measurement. The Gaussian function is shown in Figure 38.

Continuing on the logic that the surface current field contains information which is relevant to the surface SST field, the interpolation weighting function might be modified based on existing current measurements. For example, the weighting function can be adaptively stretched to weigh measurements which lie along local current vectors more than measurements which lie perpendicular to the local current vectors. This interpolation function can be changed for each location on the map based on local current information. Figure 39 shows a interpolation weighting function based on the Gaussian function which has been compacted in the x direction.

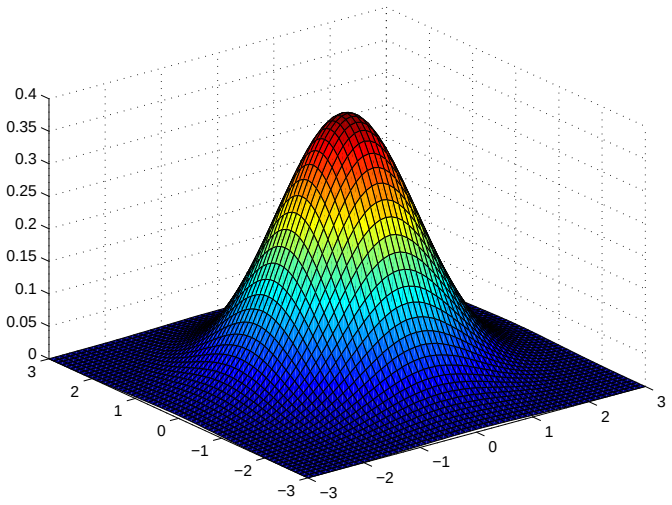

Figure 38. Gaussian weighting function.

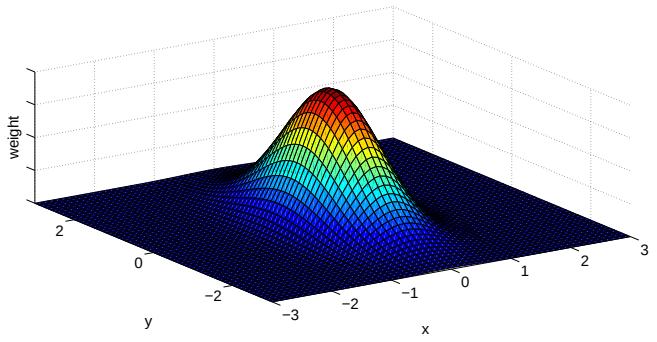

Figure 39. Gaussian weighting function, slimmed in the x direction.

5. Improvements to Current Fits from OMA Method

Additional work remains on the OMA method. Improvements can be made to fitting OMA modes to existing current measurements. In this investigation, the only measurements used to fit OMA modes originate from the CODAR HF radars. Other current measurements exist which can be used to fit OMA modes, although care should be taken to ensure that the ocean depth at which currents are measured are compatible across different measurement instruments. For example, current instruments on moored ocean buoys can be used in OMA fits, as well as currents from tidal gauges. Currents near land are hard for the HF radars to measure, but can play a large part in current circulation patterns, especially in bays and other inlets.

APPENDIX.

Data from the satellite passes in Tables III and IV were used in this thesis.

Date	Time(GMT)	Satellite
09	19:10:00	NOAA17
12	18:01:00	NOAA17
12	21:28:00	NOAA18
13	19:18:00	NOAA17
14	06:37:00	NOAA17
14	18:55:00	NOAA17
14	21:08:00	NOAA18
15	18:32:00	NOAA17
15	20:57:00	NOAA18
17	19:26:00	NOAA17
17	20:36:00	NOAA18
21	10:11:00	NOAA18
21	19:34:00	NOAA17
22	19:11:00	NOAA17
22	21:26:00	NOAA18
23	18:48:00	NOAA17
23	21:15:00	NOAA18
24	18:25:00	NOAA17
24	21:05:00	NOAA18

Table III. Satellite Images used in the January, 2007 Case Study

Date	Time(GMT)	Satellite
17	21:18:00	NOAA18
18	19:21:00	NOAA17
18	21:08:00	NOAA18
19	18:58:00	NOAA17
19	20:57:00	NOAA18
21	18:12:00	NOAA17
21	20:37:00	NOAA18
25	21:36:00	NOAA18
26	19:37:00	NOAA17
26	21:26:00	NOAA18
27	21:16:00	NOAA18

Table IV. Satellite Images used in the October, 2006 Case Study

LIST OF REFERENCES

[1] J.D. Paduan and H.C. Graber. Introduction to high-frequency radar: reality and myth. *Oceanography*, 10(2):36–39, 1997.

[2] S. Pond and G.L. Pickard. *Introductory Dynamical Oceanography*. Pergamon Press, New York, 2^{nd} edition, 1983, p. 212.

[3] J.D. Paduan, K.C. Kim, M.S. Cook, and F.P. Chavez. Calibration and validation of direction-finding high-frequency radar ocean surface current observations. *IEEE Journal of Oceanic Engineering*, 31(4):862–875, October 2006.

[4] H.C. Graber, B.K. Haus, L.K. Shay, and R.D. Chapman. HF radar comparisons with moored estimates of current speed and direction: Expected differences and impications. *Journal of Geophysical Research*, 102:18749 – 18766, 1997.

[5] K.W. Gurgel. Shipborne measurement of surface current fields by HF radar. *L'Onde Electrique*, 74(5):54–59, Septembre - Octobre 1994.

[6] D.C. Montgomery, E.A. Peck, and G.G. Vining. *Introduction to Linear Regression Analysis*. John Wiley & Sons, Inc., 4^{th} edition, 2006, p. 76.

[7] D.M. Kaplan and F. Lekien. Spatial interpolation and filtering of surface current data based on open-boundary modal analysis. *Journal of Geophysical Research*, 112(C12007), 2007, doi:10.1029/2006JC003984.

[8] F. Lekien, C. Coulliette, R. Bank, and J. Marsden. Open-boundary modal analysis: Interpolation, extrapolation, and filtering. *Journal of Geophysical Research*, 109(C12004), 2004, doi:10.1029/2004JC02323.

[9] H. Stommel. The westward intesification of wind-driven ocean currents. *Transactions, American Geophysical Union*, 29(2):202–206, April 1948.

[10] J.D. Paduan and L.K. Rosenfeld. Remotely sensed surface currents in monterey bay from shore-based HF radar (coastal ocean dynamics application radar). *Journal of Geophysical Research*, 101(C9):20669 – 20686, September 1996.

[11] J.R. Dormand and P.J. Prince. A family of embedded runge-kutta formulae. *Journal of Computational and Applied Mathematics*, 6:19–26, 1980.

[12] S.C. Shadden, F. Lekien, J.D. Paduan, F.P. Chavez, and J.E. Marsden. The correlation between surface drifters and coherent structures based on high-frequency radar data in monterey bay. *Deep Sea Research*, in press.

THIS PAGE INTENTIONALLY LEFT BLANK

INITIAL DISTRIBUTION LIST

1. Defense Technical Information Center
   Fort Belvoir, Virginia

2. Dudley Knox Library
   Naval Postgraduate School
   Monterey, California

3. Francis X. Giraldo
   Naval Postgraduate School
   Monterey, California

4. Clyde Scandrett
   Naval Postgraduate School
   Monterey, California

5. Jeffrey Paduan
   Naval Postgraduate School
   Monterey, California

6. Franklin Schwing
   Environmental Research Division Southwest Fisheries Science Center
   National Oceanic and Atmospheric Administration
   Pacific Grove, California

7. David Foley
   NOAA CoastWatch, West Coast Regional Node
   Pacific Grove, California

8. David Kaplan
   Institut de Recherche pour le Developpement
   Centre de Recherche Halieutique Mediterraneenne et Tropicale
   Paris, France

9. Chris Edwards
   University of California Santa Cruz
   Santa Cruz, California

10. Raphael Kudela
    University of California Santa Cruz
    Santa Cruz, California

11. Chris Halle
    University of California Davis
    Davis, California

12. Milena Veneziani
    University of California Santa Cruz
    Santa Cruz, California

13. Newell Garfield
    San Francisco State University
    San Francisco, California